

Coupling the Level Set Method to Moments and Particles for Computing N-phase flows with phase change.

, , , ,

Abstract

A new algorithm that hybridizes marker particles with the coupled level set moment-of-fluid method to improve the interface reconstruction in N-phase flow problems is proposed. This approach uses both near and on-interface Lagrangian marker particles to improve the slope reconstruction for the multimaterial moment of fluid (MOF) method. Deriving the MOF slopes from particles overcomes the surface tension checkerboard instability of the MOF method, first discussed by Ye et al. (2023). Ye et al. developed the Continuous Moment of Fluid (CMOF) method in order to overcome this checkerboard instability. The coupled particle moment of fluid method (PMOF) method proposed herein is compared to both MOF and CMOF on rigid body tests and multiphase flow problems in 2D, axisymmetric “R-Z”, and 3D coordinate systems. Examples include two and three material multiphase flows, with and without phase change: bubble formation, liquid lens dynamics, freezing droplet on a cold substrate, and an impinging liquid jet on vapor ullage in a cryogenic tank. It has been found that augmenting the interface representation with meshless particle produces similar results to that of the CMOF method, at a computational cost similar to that of MOF. The proposed method is volume-preserving and generalizable to unstructured grids.

Keywords: Moment-of-Fluid (MOF), Level Set, Particles, Surface tension, Phase change, Multimaterial, Multiphase, N-phase flow

1. Introduction

Incompressible multiphase flow and encapsulation simulations using the moment-of-fluid method, Li, Guibo and Lian, Yongsheng and Guo, Yisen and Jemison, Matthew and Sussman, Mark and Helms, Trevor and Arienti, Marco

An Improved Coupled Level Set and Continuous Moment-of-Fluid Method for Simulating Multiphase Flows with Phase Change, Ye, Zhouteng and Estebe, Cody and

Liu, Yang and Vahab, Mehdi and Huang, Zeyu and Sussman, Mark and Moradikazerooni, Alireza and Shoele, Kourosh and Lian, Yongsheng and Ohta, Mitsuhiro and Hussaini, M. Yousuff

Fluid-structure interaction of thin flexible bodies in multi-material multi-phase systems Mehdi Vahab and Mark Sussman and Kourosh Shoele

FabricMask paper

A boundary condition capturing method for multiphase incompressible flow Kang, Myungjoo and Fedkiw, Ronald P and Liu, Xu-Dong

MOF Reconstruction

checkerboard instability

CMOF Reconstruction

Decision tree table time consuming to build, not generalizable to unstructured grids.

PLSMOF Reconstruction

Show results and animations: liquid lens, gas lens, tank, freezing

add table: existing multiphase flow MOF methods with surface tension, report curvature algorithm

Authors	Curvature Discretization	N-phase	Interface Representation	grid
Kumaran et al. 2024 [21]	height function	2	sharp	staggered, unstructured
Pan et al. 2024 [15]	height function	2	sharp, front tracking	staggered, structured
Mukundan et al. 2020 [14]	Level Set	2	sharp	staggered, structured
Li et al. 2015[10]	height function	≥ 2	sharp	staggered, structured

Table 1: Recent Multimaterial MOF papers and their curvature discretizations.

Authors	Curvature Discretization	N-phase	Interface Representation	grid
Kumaran et al. CITE				
Mukundan et al. 2020 [14]	Level Set			
Li et al.[10]	Height Function			

2. Mathematical Model

$$\phi_{m_{\text{rigid}}}(\mathbf{x}, t) = \begin{cases} > 0 & \mathbf{x} \in \text{material } m_{\text{rigid}}, \\ \leq 0 & \text{otherwise,} \end{cases} \quad (1)$$

$$\phi_{m_{\text{fluid}}}(\mathbf{x}, t) = \begin{cases} > 0 & \mathbf{x} \in \text{material } m_{\text{fluid}} \cup m_{\text{fluid,ghost}}, \\ \leq 0 & \text{otherwise.} \end{cases} \quad (2)$$

$$\phi_{m_1, m_2}(\mathbf{x}, t) = \begin{cases} > 0 & \mathbf{x} \in \text{material } m_1, \\ < 0 & \mathbf{x} \in \text{material } m_2, \\ = 0 & \text{for } \mathbf{x} \text{ along } (m_1, m_2) \text{ interface.} \end{cases} \quad (3)$$

The multiphase system is comprised of M_{fluid} deforming materials and M_{rigid} non-deforming materials. The fluid materials tessellate the entire computational domain (extended through any rigid bodies), and where a material m_{fluid} intersects with a solid m_{rigid} region, the governing equations for the rigid body is used. In regions not containing a m_{rigid} , the incompressible Navier-Stokes equations of immiscible flows govern the fluid materials.

3. Governing Equations

3.1. Multimaterial Level Sets

We define the rigid and fluid materials using the following multimaterial level set formulation:

$$\phi_{m_{\text{rigid}}}(\mathbf{x}, t) = \begin{cases} > 0 & \mathbf{x} \in \text{material } m_{\text{rigid}}, \\ \leq 0 & \text{otherwise,} \end{cases} \quad (4)$$

$$\phi_{m_{\text{fluid}}}(\mathbf{x}, t) = \begin{cases} > 0 & \mathbf{x} \in \text{material } m_{\text{fluid}} \cup m_{\text{fluid,ghost}}, \\ \leq 0 & \text{otherwise.} \end{cases} \quad (5)$$

For position vector \mathbf{x} and time t . Material m_{rigid} is defined as the region where $\phi_{m_{\text{rigid}}} > 0$ and the domain of material m_{fluid} as the region where $\phi_{m_{\text{fluid}}} > 0$ and $\phi_{m_{\text{rigid}}} < 0$. m_{ghost} indicates the region in which the fluid level set is extended through the rigid body. This extension is implemented as in [1] in which the fluid interface is extended orthogonally to the rigid body, regardless of contact angle. This configuration can be seen in figure 1 below.

The interface level set, ϕ_{m_1, m_2} , represents the interface between materials m_1 and m_2

$$\phi_{m_1, m_2}(\mathbf{x}, t) = \begin{cases} > 0 & \mathbf{x} \in \text{material } m_1, \\ < 0 & \mathbf{x} \in \text{material } m_2, \\ = 0 & \text{for } \mathbf{x} \text{ along } (m_1, m_2) \text{ interface.} \end{cases} \quad (6)$$

The interfacial level sets are not stored nor extended through the material level sets as in [25]. Where needed, we instead obtain the interfacial level sets from the involved material level sets as

$$\phi_{m_1, m_2} = \frac{\phi_{m_1} - \phi_{m_2}}{2}. \quad (7)$$

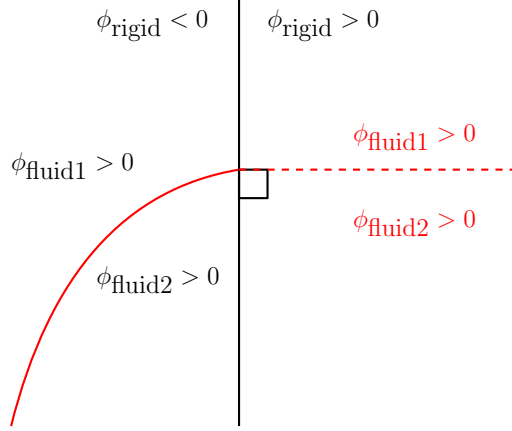


Figure 1: fluid level set extension through rigid region

The associated normal \mathbf{n} and curvature κ for the level set functions are defined as

$$\mathbf{n}_{m_1, m_2} = \frac{\nabla \phi_{m_1, m_2}}{\|\nabla \phi_{m_1, m_2}\|}, \quad \kappa_{m_1, m_2} = \nabla \cdot \frac{\nabla \phi_{m_1, m_2}}{\|\nabla \phi_{m_1, m_2}\|}. \quad (8)$$

3.2. Conservation of mass

Each fluid material, m_{fluid} , is assumed to be incompressible, so that the velocity field \mathbf{u} is divergence free within each fluid material:

$$\nabla \cdot \mathbf{u} = 0. \quad (9)$$

The following conditions on $\nabla \cdot \mathbf{u}$ are enforced to account for phase change and any mass sources or sinks:

$$\nabla \cdot \mathbf{u} = \sum_{\text{sources}} \frac{\dot{m}_{\text{source}}}{\rho_{\text{source}}} \delta(\phi_{m_{\text{source}}}) - \sum_{\text{sinks}} \frac{\dot{m}_{\text{sink}}}{\rho_{\text{sink}}} \delta(\phi_{m_{\text{sink}}}) \quad (10)$$

where $\delta(\phi)$ is the Dirac delta function,

$$\delta(\phi) = H'(\phi) \quad (11)$$

and $H(\phi)$ is the Heaviside function,

$$H(\phi) = \begin{cases} 1 & \phi > 0 \\ 0 & \phi \leq 0. \end{cases} \quad (12)$$

\dot{m} is the mass flux. For the mass flux of boiling liquid across the liquid/vapor interface, we have

$$\dot{m} = \frac{k_l \nabla T_l \cdot \mathbf{n}_{l,v} - k_v \nabla T_v \cdot \mathbf{n}_{l,v}}{L}, \quad (13)$$

where k_l and k_v are the respective thermal conductivities of the liquid and ambient vapor regions. ρ_l and ρ_v are the respective densities of the liquid and ambient vapor regions. L is the latent heat of vaporization. Vector $\mathbf{n}_{l,v}$ is the interface normal that points from the vapor region into the liquid,

$$\mathbf{n}_{l,v} = \frac{\nabla \phi_{l,v}}{\|\nabla \phi_{l,v}\|}. \quad (14)$$

3.3. Conservation of momentum:

For each material in its domain $\phi_m(\mathbf{x}, t) > 0$ we have the following conservation of momentum:

$$(\mathbf{u}\rho_m)_t + \nabla \cdot (\mathbf{u} \otimes \mathbf{u}\rho_m + p_m \mathbb{I}) = \nabla \cdot (2\mu_m \mathbb{D}) + \rho_m \mathbf{g}(1 - \alpha_m(T_m - T_{0m})). \quad (15)$$

with density ρ_m , pressure p_m , temperature T_m , coefficients of thermal expansion α_m , and viscosities μ_m for material m . \mathbf{g} is the acceleration due to gravity and $\mathbb{D} = \frac{1}{2}(\nabla \mathbf{u} + (\nabla \mathbf{u})^T)$ is the rate of deformation tensor.

3.4. Conservation of energy:

For each material in its domain $\phi_m(\mathbf{x}, t) > 0$ we have the conservation of energy equation:

$$(\rho_m C_{p,m} T_m)_t + \nabla \cdot (\mathbf{u}\rho_m C_{p,m} T_m) = \nabla \cdot (k_m \nabla T_m). \quad (16)$$

$C_{p,m}$ is the heat capacity, k_m is the thermal conductivity, and T_m is the temperature corresponding to material m .

3.5. Interfacial jump conditions:

We represent a deforming interface undergoing phase change with the following general equations.

$$\phi_{m_s, m_d} + \mathbf{u}_{m_s} \cdot \nabla \phi_{m_s, m_d} = -\frac{\dot{m}}{\rho_s} \|\nabla \phi_{m_s, m_d}\| \quad (17)$$

$$\phi_{m_d, m_s} + \mathbf{u}_{m_s} \cdot \nabla \phi_{m_d, m_s} = \frac{\dot{m}}{\rho_s} \|\nabla \phi_{m_d, m_s}\| \quad (18)$$

Or, equivalently:

$$\phi_{m_s, m_d} + \mathbf{u}_{m_d} \cdot \nabla \phi_{m_s, m_d} = -\frac{\dot{m}}{\rho_d} \|\nabla \phi_{m_s, m_d}\| \quad (19)$$

$$\phi_{m_d, m_s} + \mathbf{u}_{m_d} \cdot \nabla \phi_{m_d, m_s} = \frac{\dot{m}}{\rho_d} \|\nabla \phi_{m_d, m_s}\| \quad (20)$$

For the level set ϕ_{m_s, m_d} indicating the interface separating a material m_s region from a material m_d region. m_s is defined as the material id associated with a ‘source’ material and m_d is the corresponding ‘destination’ material (e.g. for boiling, m_s is the liquid material and m_d the vapor region and for freezing, m_s would indicate the liquid material and m_d the icing material).

For the velocity, pressure, and temperature interface jump conditions between materials m_s and m_d , we apply the following definitions:

$$\mathbf{u}_{m_s} \cdot \mathbf{n}_{m_s, m_d} - \mathbf{u}_{m_d} \cdot \mathbf{n}_{m_s, m_d} = \dot{m} \left(\frac{1}{\rho_{m_d}} - \frac{1}{\rho_{m_s}} \right), \quad (21)$$

$$(p_{m_s} \mathbb{I} - p_{m_d} \mathbb{I}) \cdot \mathbf{n}_{m_s, m_d} = -\sigma_{m_s, m_d} \kappa_{m_s, m_d} \mathbf{n}_{m_s, m_d} + (2\mu_{m_s} \mathbb{D}_{m_s} - 2\mu_{m_d} \mathbb{D}_{m_d}) \cdot \mathbf{n}_{m_s, m_d}, \quad (22)$$

$$T_{m_s} = T_{m_d}. \quad (23)$$

Where σ_{m_s, m_d} is the prescribed surface tension and κ_{m_s, m_d} is the interface curvature, defined as

$$\kappa_{m_s, m_d} = \nabla \cdot \frac{\nabla \phi_{m1, m2}}{\|\nabla \phi_{m1, m2}\|}. \quad (24)$$

3.6. Triple point junction

At a triple point, a three-phase equilibrium (Neumann’s triangle [6]) determines the contact angles for a steady state, dependent on the surface tension of the phases in contact. (see Figure 2(a)):

$$\frac{\sin(\theta_1)}{\sigma_{23}} = \frac{\sin(\theta_2)}{\sigma_{13}} = \frac{\sin(\theta_3)}{\sigma_{12}}. \quad (25)$$

4. Numerical Method

4.1. Interface Reconstruction

4.1.1. Moment-of-Fluid reconstruction

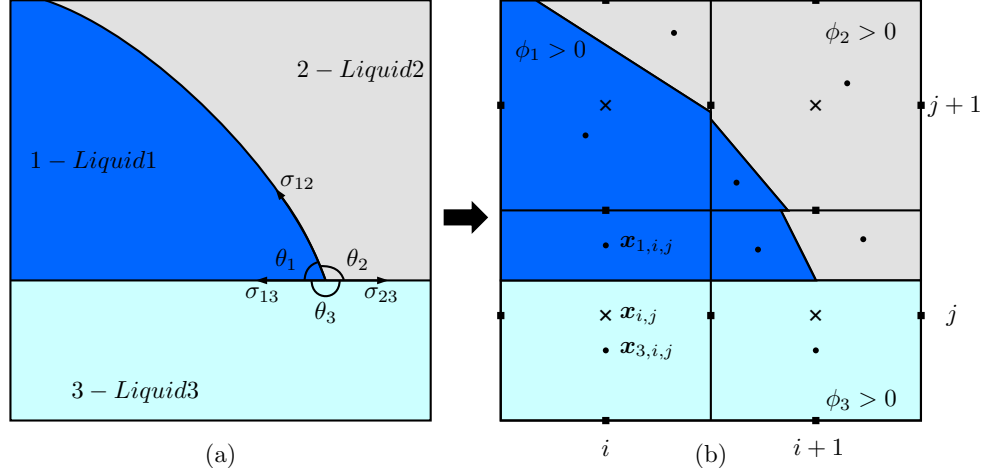


Figure 2: (a) Physical Domain, shown here for a triple point. The contact angles θ are determined at equilibrium by the surface tension forces σ .

(b) Discretized Domain. \times : cell centers, \bullet : cell centroids, \blacksquare : MAC velocities

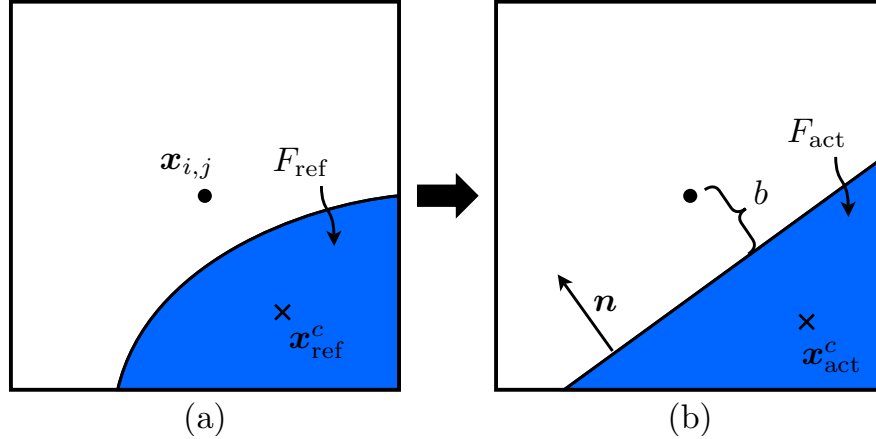


Figure 3: (a) Material domain in a cell $\Omega_{i,j}$, a single phase shown in blue corresponding with reference volume F_{ref} and centroid \mathbf{x}_{ref}^c .

(b) The piecewise linear MOF reconstruction. The line segment for the reconstructed volume can be represented as $\Omega_{i,j} \cap \{\mathbf{x} | \mathbf{n} \cdot (\mathbf{x} - \mathbf{x}_{i,j}) + b = 0\}$.

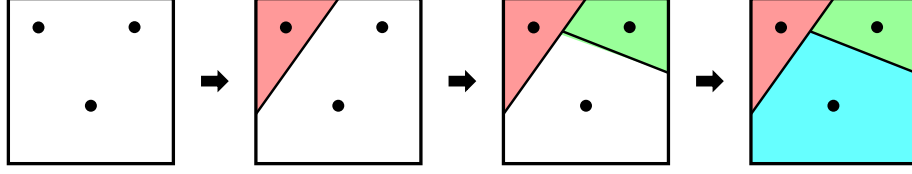


Figure 4: MOF reconstruction, volume-tessellation (nested dissection) procedure. Points indicate centroids, white space is the unoccupied region, and zones of color indicate reconstructed materials.

4.1.2. Continuous MOF reconstruction

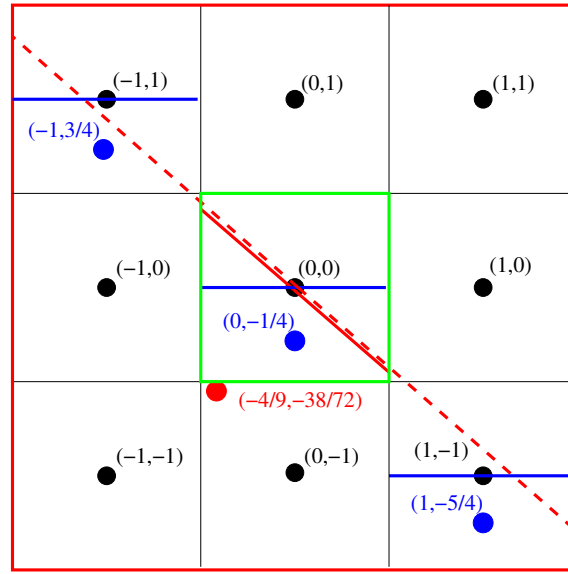


Figure 5: CMOF reconstruction. Black dots represent cell centroids, blue dots represent ‘material 1’ centroids, and the red dot represents the CMOF supercell (red boundary) centroid associated with the center cell (green boundary) for ‘material 1’. The CMOF reconstructed interface (solid red line inside the center cell) is found such that it is the line segment which minimizes the difference between the CMOF reference centroid (red dot) and the CMOF derived centroid (centroid associated with the dashed red line) subject to the constraint that the reference MOF volume fraction (‘material 1’ volume fraction within the center cell) equals the actual CMOF reconstructed volume fraction (‘material 1’ volume fraction below the solid red line in the center cell).

4.1.3. Particle Level Set MOF reconstruction

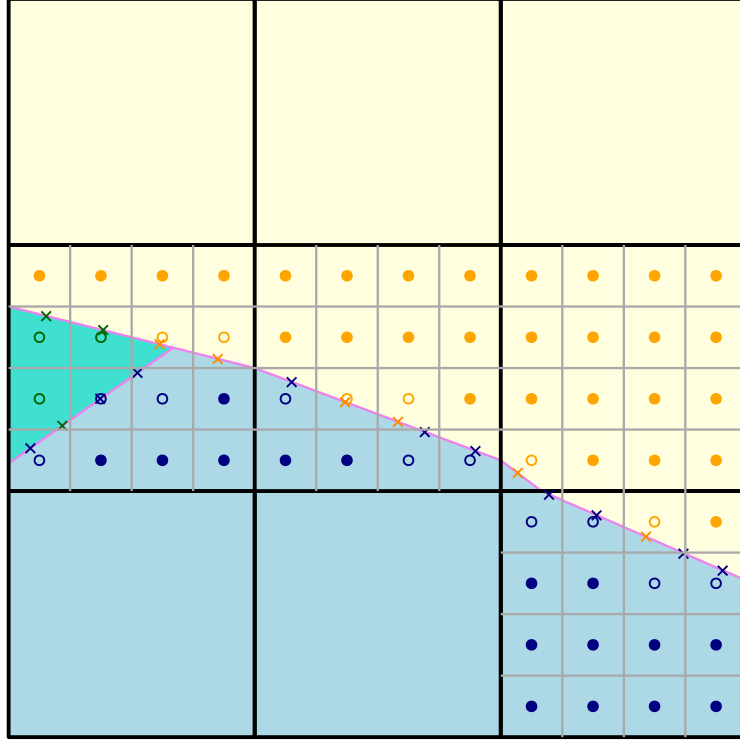


Figure 6: subdividing cell, $N = 4$, grid lines: Δx_{sub} . \bullet : near-interface particles, \times : on-interface particles, \bigcirc : cell-centers for particle sent to interface, color indicates associated material

4.2. Redistancing

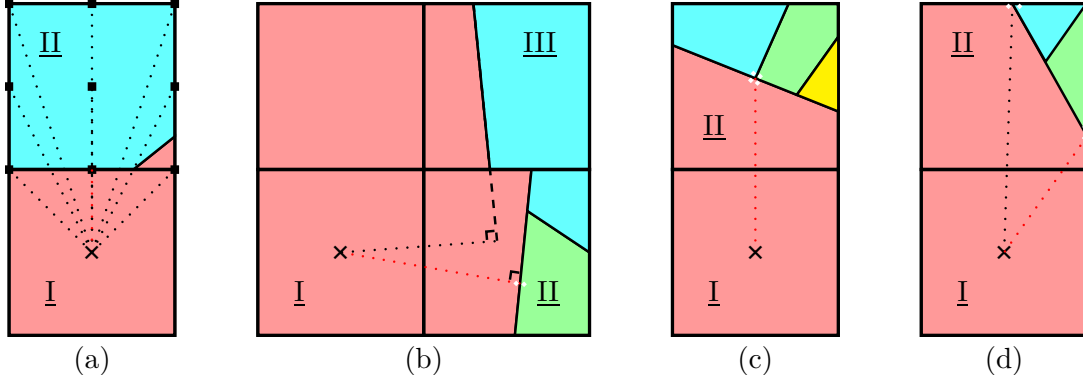


Figure 7: MOF redistancing procedure (shown for candidate cell-center \times in update cell I).

(a) Candidate distances (black dotted lines) are measured from the center of update cell (I) to the center, corners, and faces of the support cell (II). In this configuration, the nearest sample point coinciding with a different material is indicated by the red dotted line. If the material interface coincides with the cell boundary, this gives the exact distance.

(b) The distance between update cell (I) using the reconstructed normal for the interface in support cell (II) is shown by the red dotted line. Since the intersection point is contained within the support cell, the two material ids are obtained using test points (white dots) on both sides. In this example, the signed distance and corresponding normal vector for the red material level set, green material level set, and red-green interface level sets are updated. Note: The candidate normal distance with support cell (III) is shown by the black dotted line. Since the intersection point is not contained within the support cell, this distance is not accepted.

(c) The distance between update cell (I) and the material intersections in support cell (II) is measured (red dotted line). Test points (white dots) around the triple point are used to find the material ids. In this example, the red, blue, and green material level sets are updated and the red-blue, red-green, and blue-green interface level sets are updated. Similarly for the red-green-yellow triple point.

(d) Distances between update cell (I) and the cell face intersections in support cell (II) is shown. Test points and level set updates follow as in (c). In this example, red and blue material level sets and blue-red interface level sets are updated (black dotted line) and similarly for red and green.

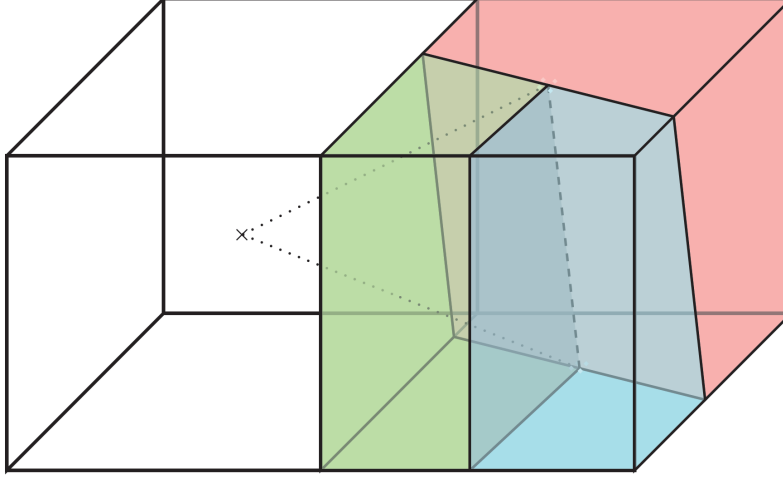


Figure 8: 3D MOF redistancing. Update cell (left), querying normal distances to potential nearest interface plane intersection (black dashed line) within support cell (right) as well as distances to the line formed by the intersection of the interface plane with the cell boundaries.

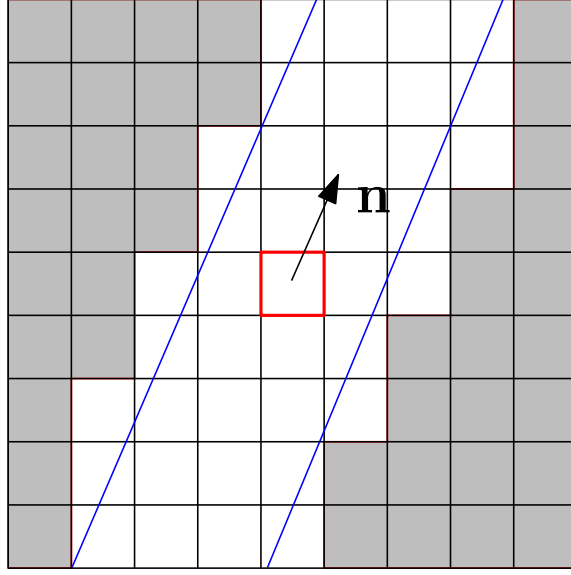


Figure 9: The reduced neighborhood stencil. The red cell indicates a support cell about which we construct a $9 \times 9(\times 9)$ update neighborhood. The blue lines indicate the reduced band (3 cells thick), aligned in the direction of the interface normal. The grey regions indicate the parts of the $9 \times 9(\times 9)$ stencil that lie outside the narrow band reduction that are not evaluated. If the normal is oriented with the grid, the neighborhood stencil is reduced to a $3 \times 9(\times 3)$ region.

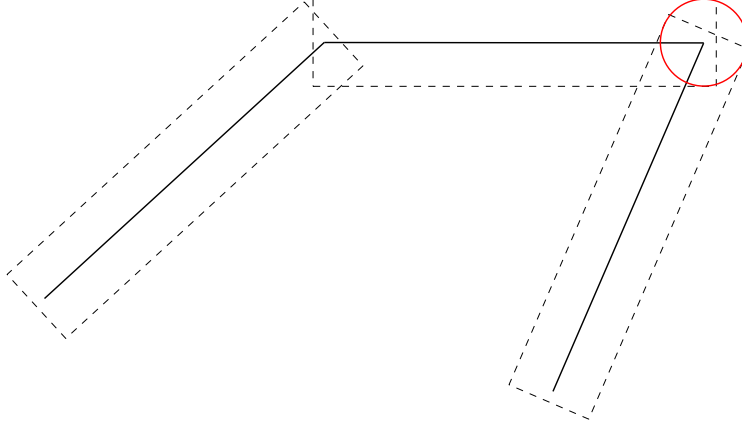


Figure 10: The maximum extent of the stencil-covered region of each piecewise linear interface segment is indicated by the dashed lines. At the end of the linear segments, the update region does not extend the full thickness of the narrow band due to the orientation of the stencils. This may produce regions for which cells are within the narrow band but not updated during the redistancing step. This can be seen at the junctions of the linear segments (a small gap off the left junction and a larger one on the right, the red circle is centered at a junction with the radius indicating the width of the narrow band). Directly near the end of the linear segment, cells are still guaranteed to be updated due to the stencil thickness, but further away, regions may form in which cells do not get redistanced. Since the cells in the gap region that lie farther from the interface are not updated, the error from these may pollute the level set function and therefore eventually the slopes and volume fractions. However, in practice the error introduced is found to be negligible and the speedup from the stencil reduction significant. In addition to remaining sufficiently accurate, this reduction does not affect the linearity preserving property of the reconstruction (the method is exact for piecewise linear interfaces).

4.3. Staggered Grid Projection Method

Outline of the operator-split staggered grid projection method:

1. Find the time step $\Delta t = t^{n+1} - t^n$:

$$\begin{cases} \Delta t_1 &= \min_{d=1,\dots,\dim} \frac{\min \Delta x_d}{2(\dim) \max ||u_d^n||} \\ \Delta t_2 &= \min_{d=1,\dots,\dim} \frac{\min \Delta x_d}{(\dim) \max ||u_d^{\text{phase change},n-1}||} \\ \Delta t_3 &= \min_{d=1,\dots,\dim} \min_{m_1,m_2=1,\dots,M} \Delta x_d^{3/2} \sqrt{\frac{\rho_{m_1} + \rho_{m_2}}{2\pi\sigma_{m_1,m_2}}} \end{cases} \quad (26)$$

$$\Delta t = \text{CFL} \min(\Delta t_1, \Delta t_2, \Delta t_3) \quad (27)$$

where ‘dim’ is the dimension of the problem (2 or 3). We let the coefficient ‘CFL’ = $\frac{1}{2}$. The time step is restricted by the CFL conditions on the MAC velocity, the rate of phase change, and surface tension.

Ghost Fluid Method for surface tension [9]:

$$\frac{p_{I,L} - p_L}{\rho_L \theta_L \Delta x} = \frac{p_R - p_{I,R}}{\rho_R \theta_R \Delta x}$$

$$p_{I,R} - p_{I,L} = -\sigma \kappa$$

$$\frac{p_{I,R} + \sigma \kappa - p_L}{\rho_L \theta_L \Delta x} = \frac{p_R - p_{I,R}}{\rho_R \theta_R \Delta x}$$

$$p_{I,R} \left(\frac{1}{\rho_L \theta_L \Delta x} + \frac{1}{\rho_R \theta_R \Delta x} \right) = \frac{p_L}{\rho_L \theta_L \Delta x} + \frac{p_R}{\rho_R \theta_R \Delta x} - \frac{\sigma \kappa}{\rho_L \theta_L \Delta x}$$

$$\rho_f \equiv \rho_L \theta_L + \rho_R \theta_R$$

$$p_{I,R} \rho_f = p_L \rho_R \theta_R + p_R \rho_L \theta_L - \sigma \kappa \rho_R \theta_R$$

$$\frac{p_R \rho_f - p_{I,R} \rho_f}{\rho_f \rho_R \theta_R \Delta x} =$$

$$\frac{p_R \rho_R \theta_R - p_L \rho_R \theta_R + \sigma \kappa \rho_R \theta_R}{\rho_f \rho_R \theta_R \Delta x} =$$

$$\frac{p_R - p_L}{\rho_f \Delta x} + \sigma \kappa \frac{1}{\rho_f \Delta x}$$

Assume

$$|\kappa| < \frac{1}{\Delta x},$$

then we want:

$$\left(\Delta t \sigma \frac{1}{\rho_f \Delta x^2} \right) \Delta t \leq \frac{1}{2} \Delta x$$

$$\Delta t \leq \Delta x^{3/2} \sqrt{\frac{\rho_f}{2\sigma}}$$

Slope reconstruction using level set function, particles, centroid and volume fraction:

$$\phi(\vec{x}) = \vec{n} \cdot (\vec{x} - \vec{x}_0) + b$$

$$(\vec{n}, b) = \operatorname{argmin} \sum_{ijk} \delta(\|\vec{x}_{ijk} - \vec{x}^c\|) (\phi(\vec{x}_{ijk}) - \phi_{ijk})^2 + \sum_p \delta(\|\vec{x}_p - \vec{x}^c\|) (\phi(\vec{x}_p) - \phi_p)^2$$

Replace the least squares b with that which is derived from the reference volume fraction F^{ref} :

$$\text{VOLFRAC}(\vec{n}, b^{ref}) = \text{VOLFRAC}^{ref}$$

4.4. Cell Integrated Semi-Lagrangian

The following Cell Integrated Semi-Lagrangian (CISL) procedures are implemented and terms discretized as in [16, 10, 22]. This method follows an operator-splitting approach. The steps listed below are solved by the conservative Weymouth and Yue [24], or alternatively, the Euler Implicit-Lagrange Explicit (EI-LE) [17, 2] directionally-split methods.

The idea behind the CISL integration is to trace the characteristics backwards of a cell being updated using in an unconditionally stable Semi-Lagrangian manner [18, 23]. From this a ‘departure’ region is constructed and mapped back to the cell and the containing volume fraction and centroid reconstructed for the updated time. For the mapping function and full CISL algorithm, the reader is referred to [10]. The CISL-MOF reconstruction is visualized in Fig. 11 for a single direction. The discretizations used for the CISL algorithm are provided below.

2. Directionally split CISL-MOF, advection of the volume fractions and centroids
For materials $m = 1, \dots, M$,

$$F_{m,t} + \nabla \cdot (\mathbf{u} F_m) = 0 \quad (28)$$

$$\mathbf{x}_{m,t}^c = \mathbf{u}(\mathbf{x}_m^c) \quad (29)$$

$$F_{m,(i,j,k)}^{n+1} = \frac{\int_{\Omega_{i,j,k}^{Depart}} \chi_m^n(\mathbf{x}) d\mathbf{x}}{\|\Omega_{i,j,k}^{Depart}\|} \quad (30)$$

$$\mathbf{x}_{m,(i,j,k)}^{c,n+1} = \frac{\int_{\mathcal{T}_{\text{CISL}}(\Omega_{m,(i,j,k)}^{Depart})} \mathbf{x} \chi_m^n(\mathcal{T}_{\text{CISL}}^{-1}(\mathbf{x})) d\mathbf{x}}{\|\mathcal{T}_{\text{CISL}}(\Omega_{m,(i,j,k)}^{Depart})\|} \quad (31)$$

Where χ_m is defined as a characteristic function such that $\chi_m(\mathbf{x}) = 1$ if $\mathbf{x} \in \Omega_{m,(i,j,k)}$, 0 otherwise. $\mathcal{T}_{\text{CISL}}$ represents the mapping function. Refer to Figure 11 for integration over the region of the backwards-traced characteristics.

3. CISL level set advection

$$\phi_{m,t} + \mathbf{u} \cdot \nabla \phi_m = 0, \quad m = 1, \dots, M \quad (32)$$

$$\phi_{m,(i,j,k)}^{n+1} = \frac{\int_{\Omega_{m,(i,j,k)}^{Depart}} \phi_m^n(\mathbf{x}) d\mathbf{x}}{\|\Omega_{i,j,k}^{Depart}\|} \quad (33)$$

4. CISL advection of the MAC velocity

$$(\rho \mathbf{u})_t + \nabla \cdot (\rho \mathbf{u} \mathbf{u}) = 0, \quad (34)$$

$$u_{i-1/2,j,k}^{n+1} = \frac{\int_{\Omega_{i-1/2,j,k}^{\text{Depart}}} \sum_{m=1}^M \rho_m \chi_m^n(\mathbf{x}) u^n(\mathbf{x}) d\mathbf{x}}{\int_{\Omega_{i-1/2,j,k}^{\text{Depart}}} \sum_{m=1}^M \rho_m \chi_m^n(\mathbf{x}) d\mathbf{x}} \quad (35)$$

$$v_{i,j-1/2,k}^{n+1} = \frac{\int_{\Omega_{i,j-1/2,k}^{\text{Depart}}} \sum_{m=1}^M \rho_m \chi_m^n(\mathbf{x}) v^n(\mathbf{x}) d\mathbf{x}}{\int_{\Omega_{i,j-1/2,k}^{\text{Depart}}} \sum_{m=1}^M \rho_m \chi_m^n(\mathbf{x}) d\mathbf{x}} \quad (36)$$

$$w_{i,j,k-1/2}^{n+1} = \frac{\int_{\Omega_{i,j,k-1/2}^{\text{Depart}}} \sum_{m=1}^M \rho_m \chi_m^n(\mathbf{x}) w^n(\mathbf{x}) d\mathbf{x}}{\int_{\Omega_{i,j,k-1/2}^{\text{Depart}}} \sum_{m=1}^M \rho_m \chi_m^n(\mathbf{x}) d\mathbf{x}} \quad (37)$$

5. CISL temperature advection (liquid and gas materials)

$$(\rho_m C_{p,m} T_m)_t + \nabla \cdot (\rho_m C_{p,m} \mathbf{u} T_m) = 0, \quad m = 1, \dots, M \quad (38)$$

6. Directionally split particle advection (2nd order Runge-Kutta)

$$\mathbf{x}_{p,t} = \mathbf{u}(\mathbf{x}_p) \quad (39)$$

4.5. Phase Change

To ensure mass conservation, it is necessary that the motion of the interface remain consistent with the mass flux across the interface. The relevant steps are outlined below, implemented from [22].

1. Redistribution of mass source (the mass flux \dot{m} is redistributed from source material m_s to destination material m_d): Eq. 13. This is implemented as follows
 - Loop through the grid, for every cell that has a valid closest point map, find if it changes phase at the corresponding closest point.
 - If it does, then \dot{m} is found:
 - $\dot{m} = \left[\frac{k \nabla T \cdot \mathbf{n}}{L} \right]$

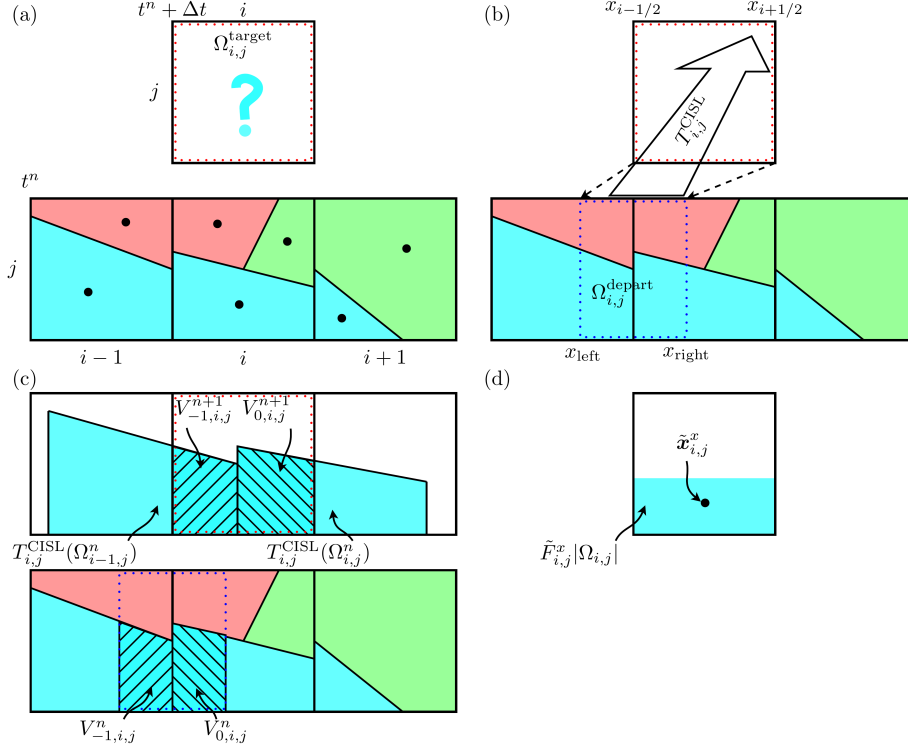


Figure 11: CISL-MOF method [figure from [16]], shown here for x -direction for the blue material.

(a) Reconstructed MOF interface and centroids at departure time t^n for slab of cells $[\{i-1, i, i+1\}, j]$ and target cell $\Omega_{i,j}^{\text{target}}$ at arrival time $t^n + \Delta t$.

(b) Characteristics are traced backwards and CISL mapping function T^{CISL} calculated.

(c) The CISL mapping function sends the material from the departure time to the update time and its intersection with the target cell is found.

(d) The contained region is combined to obtain the volume fraction and centroid

2. Phase change velocity (from source material m_s to destination material m_d).

$$\mathbf{u}^{\text{phase change}} = -\frac{\dot{m}}{\rho_{m_d}} \mathbf{n}_{m_d}, \left(\text{or } \mathbf{u}^{\text{phase change}} = \frac{\dot{m}}{\rho_{m_s}} \mathbf{n}_{m_s} \right) \quad (40)$$

3. Phase change, level set unsplit advection

$$\phi_{m,t} + \mathbf{u}^{\text{phase change}} \cdot \nabla \phi_m = 0, \quad m = m_s \text{ or } m_d. \quad (41)$$

4. Phase change: unsplit CISEL advection

$$F_{m,t} + \nabla \cdot (\mathbf{u}^{\text{phase change}} F_m) = 0, \quad m = m_s \text{ or } m_d. \quad (42)$$

$$\mathbf{x}_{m,t}^c = \mathbf{u}^{\text{phase change}}(\mathbf{x}_m^c) \quad (43)$$

5. Unsplit particle advection for phase change (1st order Forward Euler)

$$\frac{d\mathbf{x}_p}{dt} = \mathbf{u}^{\text{phase change}}(\mathbf{x}_p) \quad (44)$$

6. Thermal diffusion

$$\frac{(\rho C_{p,m})^{\text{mix},n+1}}{\Delta t^{\text{swept}}}(T_m^{n+1} - T_{\text{sat},m}) = \nabla \cdot (k_m \nabla T_m^{n+1}) \quad (45)$$

This large sparse matrix system is solved using the multigrid preconditioned conjugate gradient (MGPCG) method. (See figure 12 for the temperature gradient). Note: The temperature is stored at corresponding material centroids; as the interface shifts during phase change, a crossing time approach is used to interpolate the temperature from the old time to new centroids.[12, 22]

7. Viscosity

$$\frac{\rho^{\text{mix},n+1}}{\Delta t}(\mathbf{u}^* - \mathbf{u}^{\text{advection}}) = \nabla \cdot (2\mu \mathbb{D}^*) - \rho^{n+1}(\alpha^{n+1}(T^{n+1} - T_0))\mathbf{g} \quad (46)$$

An implicit solver is used for the viscous term $\nabla \cdot (2\mu \mathbb{D}^*)$. In this case, BiCGSTAB using a Jacobi preconditioner and red-black Gauss-Seidel smoother.

8. Pressure projection The pressure projection step is formulated using Chorin's method [4]. From the momentum equation, we have

$$\frac{\mathbf{u}^{n+1} - \mathbf{u}^*}{\Delta t} = -\frac{\nabla p^{n+1}}{\rho^{\text{MAC,mix},n+1}} + \mathbf{g} - \frac{\sum_{m=1}^M \gamma_m \kappa_m \nabla H(\phi_m)}{\rho^{\text{MAC,mix},n+1}} \quad (47)$$

On the right hand side are the viscous force, gravitational force, and surface tension force terms, respectively. Note: the surface tension force term is handled in a ghost fluid manner [7, 20]. Remark: This equation exhibits a very strong discontinuity at the triple point (in which both ∇H and κ_m behave as delta functions, proportional to $1/\Delta x$, this is further exacerbated once the divergence is taken (Eq. 48) and the whole term gains a large error proportional to $1/\Delta x^3$. However, similarly as in [3] (for an error proportional to $1/\Delta x$), it is found that since this error is localized just at the triple point, it hasn't been

observed to affect the behavior away from the triple point. In the numerical experiments, the κ_m discontinuity converges under grid refinement (future convergence studies are warranted).

Taking the divergence of both sides,

$$\frac{1}{\Delta t} \left(\nabla \cdot \mathbf{u}^{n+1} - \nabla \cdot \mathbf{u}^* \right) = \nabla \cdot \left[-\frac{\nabla p^{n+1}}{\rho^{\text{MAC,mix},n+1}} + \mathbf{g} - \frac{\sum_{m=1}^M \gamma_m \kappa_m \nabla H(\phi_m)}{\rho^{\text{MAC,mix},n+1}} \right] \quad (48)$$

From equation 10, we enforce the expansion term

$$\nabla \cdot \mathbf{u}^{n+1} = \sum_{\text{sources}} \frac{\dot{m}_{\text{source}}}{\rho_{\text{source}}} \delta(\phi_{m_{\text{source}}}) - \sum_{\text{sinks}} \frac{\dot{m}_{\text{sink}}}{\rho_{\text{sink}}} \delta(\phi_{m_{\text{sink}}}) \quad (49)$$

and use the following γ_m :

$$\gamma_{m_1} = \gamma_{m_2} = \frac{1}{2} \sigma_{m_1, m_2} \quad (50)$$

for two materials m_1, m_2 in a $3 \times 3 (\times 3)$ local stencil. If three materials m_1, m_2, m_3 , are present in the stencil, then the following terms are used instead (satisfying Eq. 25):

$$\gamma_{m_1} = \frac{1}{2} (\sigma_{m_1, m_2} + \sigma_{m_1, m_3} - \sigma_{m_2, m_3}) \quad (51)$$

$$\gamma_{m_2} = \frac{1}{2} (\sigma_{m_1, m_2} + \sigma_{m_2, m_3} - \sigma_{m_1, m_3}) \quad (52)$$

$$\gamma_{m_3} = \frac{1}{2} (\sigma_{m_1, m_3} + \sigma_{m_2, m_3} - \sigma_{m_1, m_2}) \quad (53)$$

Equation 48 can then be solved for the pressure term. BiCGSTAB using a multigrid preconditioner and red-black Gauss-Seidel smoother is used.

The velocity for the next timestep is then

$$\mathbf{u}^{n+1} = \mathbf{u}^* - \Delta t \frac{\nabla p^{n+1}}{\rho^{\text{MAC,mix},n+1}} \quad (54)$$

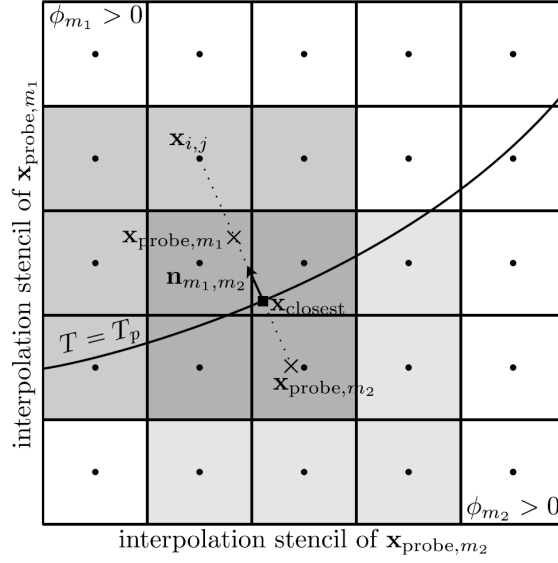


Figure 12: [figure from [22]]

The closest point is found on the interface by $x_{\text{closest}} = x_{i,j} - \phi_{m_1, m_2} \mathbf{n}_{m_1, m_2}$, two probe points are extended in either normal direction and $T(x_{\text{probe}})$ is found by interpolation.

$\nabla T_{m_1} = (T_{\text{probe}, m_1} - T_{\text{sat}, m_1, m_2}) \mathbf{n}_{m_1, m_2} / h$ and $\nabla T_{m_2} = -(T_{\text{probe}, m_2} - T_{\text{sat}, m_1, m_2}) \mathbf{n}_{m_1, m_2} / h$, where T_{sat} is the phase change saturation temperature.

5. Results

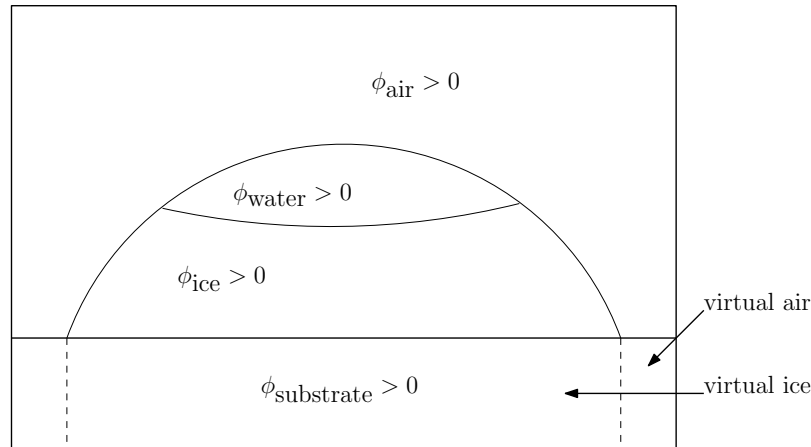


Figure 13: Initial level set construction for the problem of a water droplet freezing on top of a cold substrate. $\phi_{\text{substrate}} > 0$ in the cold substrate, $\phi_{\text{ice}} > 0$ in the ice, $\phi_{\text{water}} > 0$ in the water, and $\phi_{\text{air}} > 0$ in the rest of the domain. In this problem, only the substrate is considered a region material and is prescribed a temperature T_w . The fluid/deforming materials (ice, water, and air) tessellate the full computational domain. The orthogonal extension of the air and ice materials through the rigid substrate is indicated by the dashed lines. The ice material is handled as a deforming material rather than rigid since phase change occurs at the ice/water interface. As in the freezing model presented in [13], the ice and water are considered to be the same material during the surface tension force calculation at the triple-point where the ice, water, and air meet. That is, the interfacial curvature (both at and away from the triple point) is found using the VOF height function method [5, 10]

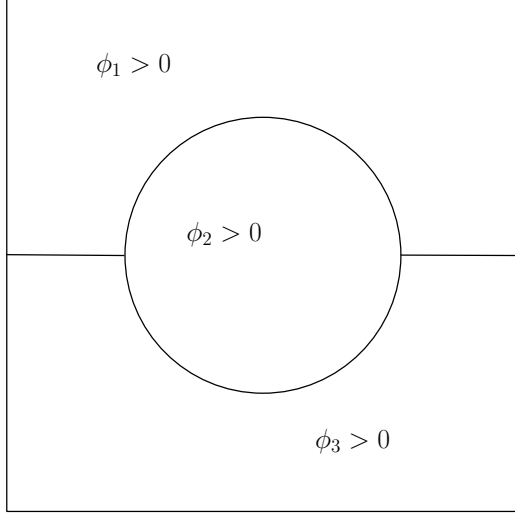


Figure 14: Initial level set construction for the simulation of a stretching ‘liquid lens’ due to surface tension. $\phi_2 > 0$ represents the lens material. ϕ_1 , ϕ_2 and ϕ_3 are all deforming fluid materials. The surface tension model described in [10], for ‘Stencil contains third fluid’ is used to calculate the surface tension forces at the triple points. This surface tension force, $\sum_{m=1}^M \gamma_m \kappa_m \nabla H(\phi_m)$, is treated using a modified ghost-fluid approach [7, 8, 20, 11] in which the curvature κ_m at the triple-point is approximated using finite differences of the level set functions ϕ . Away from triple points, the interfacial curvature is obtained by the VOF height function method [19].

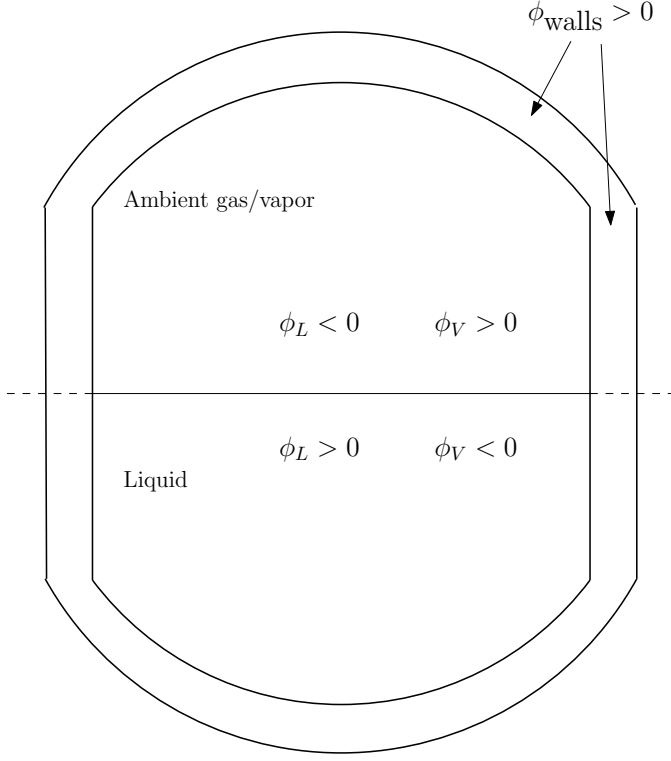


Figure 15: Initial level set functions for simulating evaporation within a cryogenic fuel tank. $\phi_{\text{walls}} > 0$ represents the rigid body of the tank which is embedded in the fluid materials. The upper vapor region $\phi_V > 0$ and the lower liquid region $\phi_L > 0$ are both extended through the tank walls to cover the full domain. The extended interface is indicated by the dashed lines. The surface tension model from [10] for ‘Stencil contains rigid boundary’ is used. The curvature at the (fluid, fluid, solid) triple-point is approximated with $\kappa = \nabla \cdot \mathbf{n}$ in which \mathbf{n} is a strategically assigned ‘ghost normal’ in the solid region, consistent with the contact angle condition. Away from the triple points, the interfacial curvature is computed with the VOF height function [19].

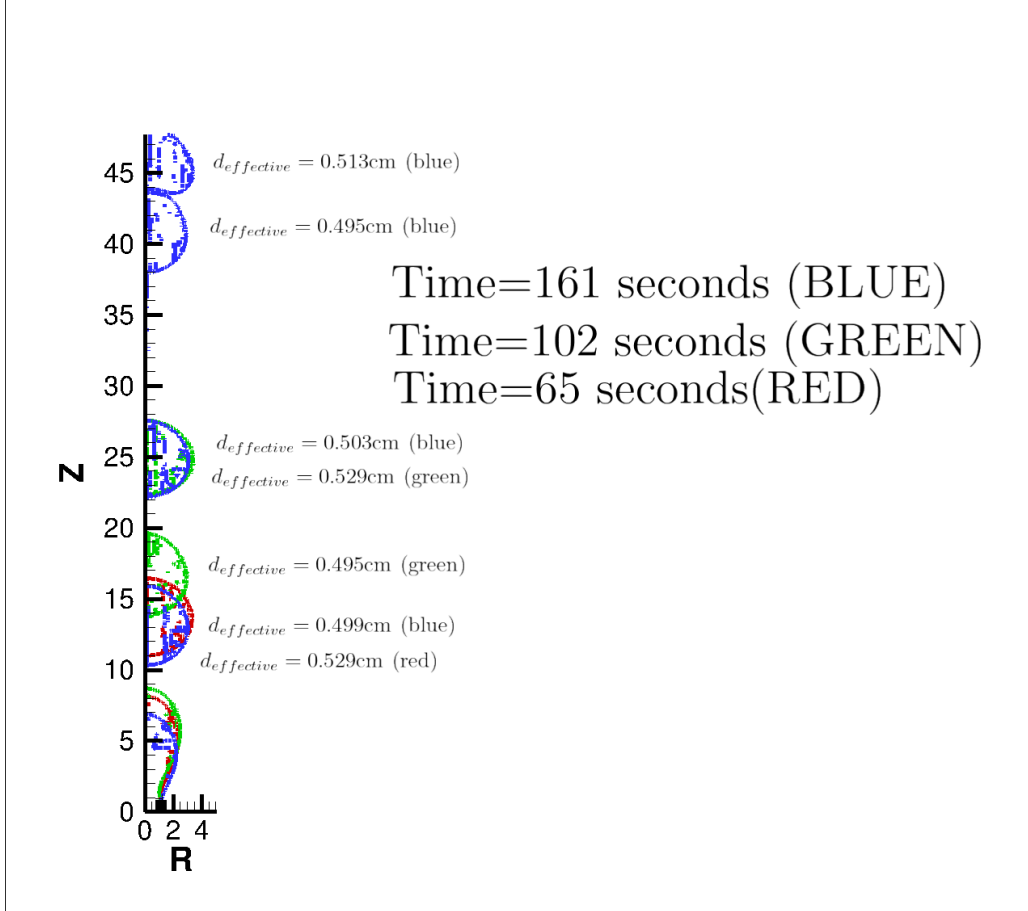


Figure 16: **MOF**, bubble formation problem.
Effective fine grid resolution : $\Delta x_{\text{fine}} = 0.010625\text{cm}$
Step numbers are 13400 ($t = 65.3$), 21600 ($t = 101.66$), and 35800 ($t = 160.7$).

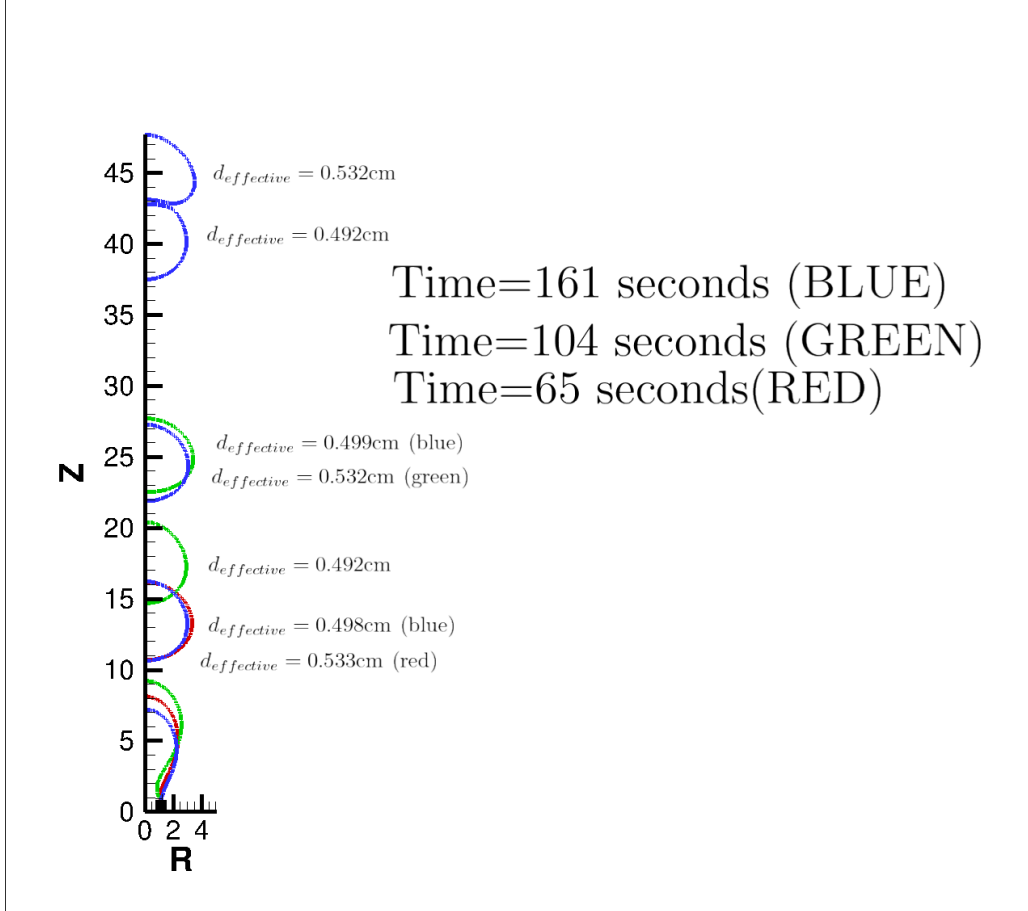


Figure 17: **CMOF**, bubble formation problem.

Effective fine grid resolution : $\Delta x_{\text{fine}} = 0.010625\text{cm}$

Step numbers are 13400 ($t = 65.3$), 21600 ($t = 103.8$), and 34200 ($t = 161.3$).

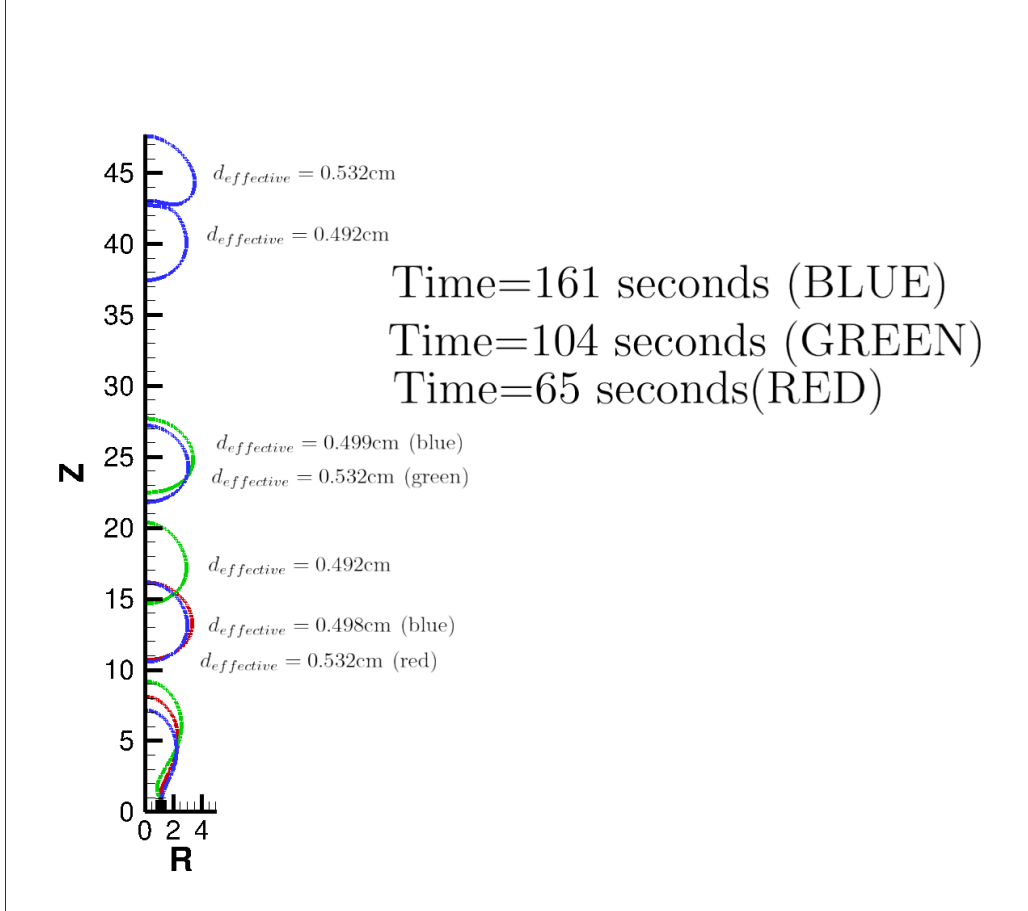


Figure 18: **PLSMOF**, bubble formation problem.

Effective fine grid resolution : $\Delta x_{\text{fine}} = 0.010625\text{cm}$

Step numbers are 13400 ($t = 65.3$), 21600 ($t = 103.8$), and 34200 ($t = 161.2$).

5.1. Bubble Formation

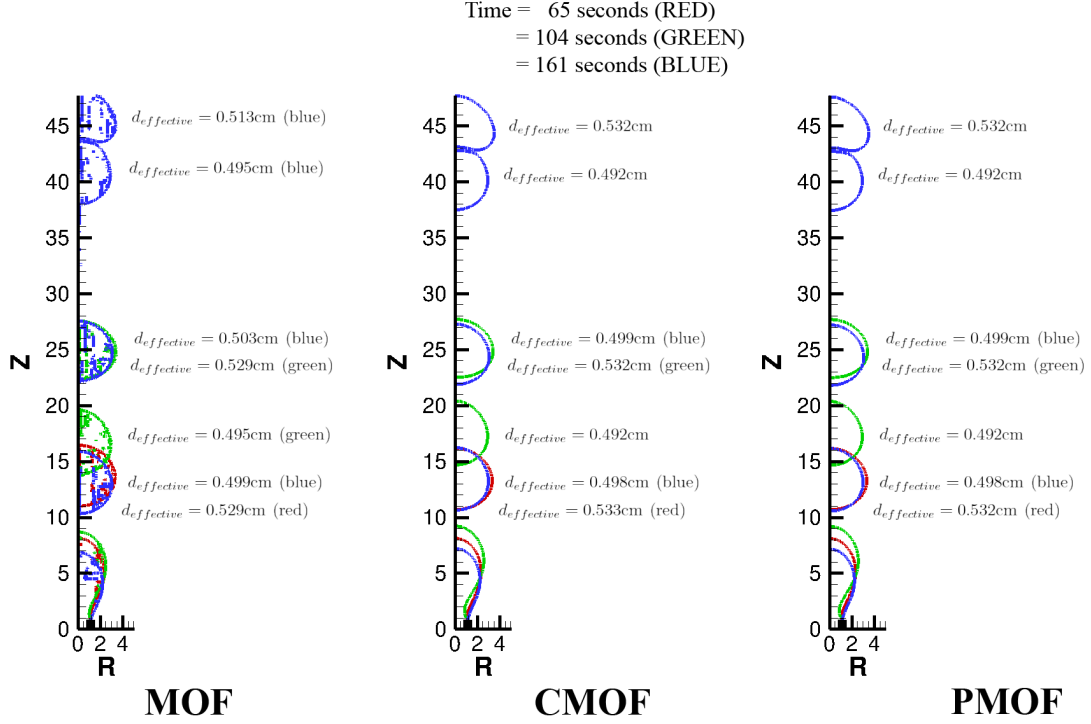


Figure 19: Bubble formation comparison.

Effective fine grid resolution : $\Delta x_{\text{fine}} = 0.010625\text{cm}$

Step numbers: (MOF) are 13400 ($t = 65.3$), 21600 ($t = 101.66$), and 35800 ($t = 160.7$).

(CMOF) are 13400 ($t = 65.3$), 21600 ($t = 103.8$), and 34200 ($t = 161.3$).

(PMOF) are 13400 ($t = 65.3$), 21600 ($t = 103.8$), and 34200 ($t = 161.2$).

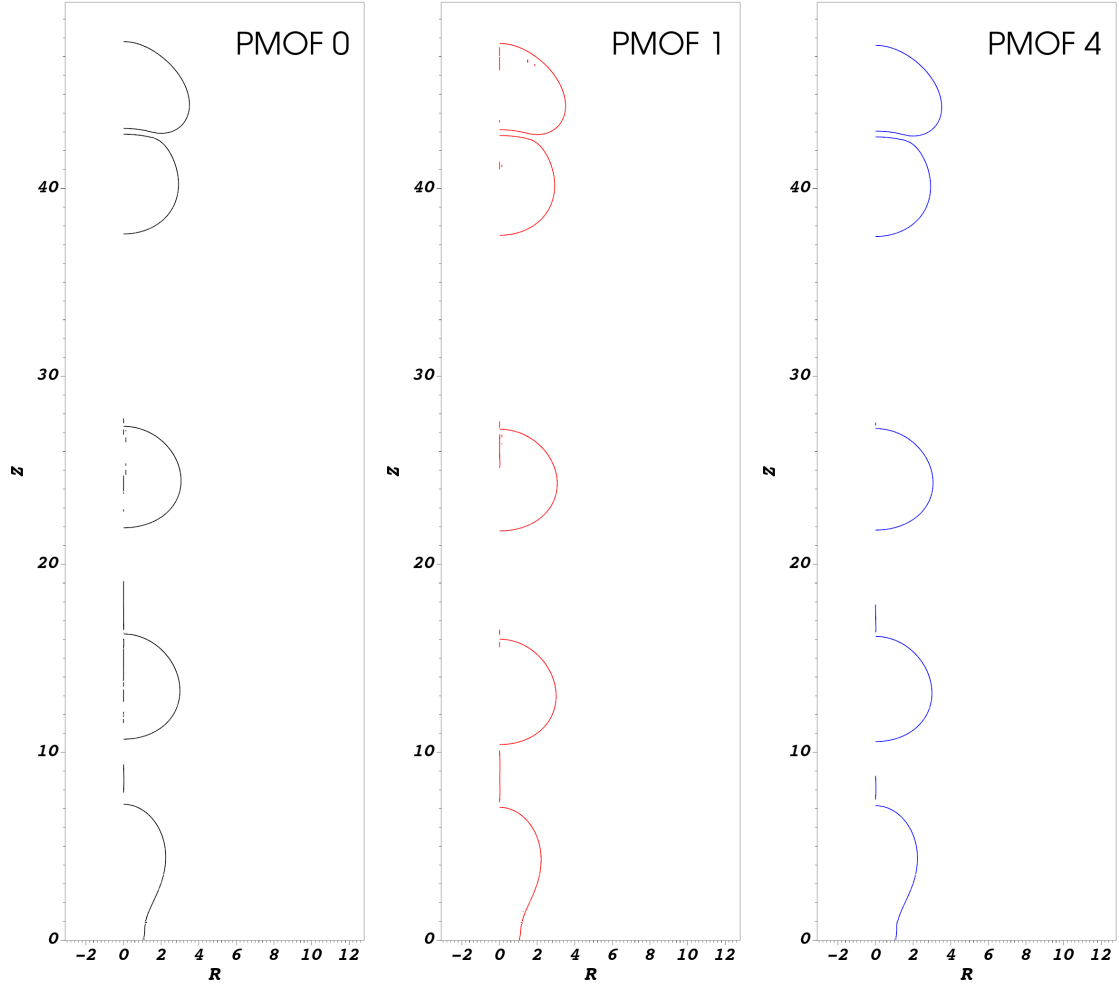


Figure 20: Bubble formation, PMOF reconstructed interface: $N = 0$ (black, $t = 161.424$), $N = 1$ (red, $t = 161.398$), $N = 4$ (blue, $t = 161.174$). Note flotsam.

5.2. Translating Disk

Table 2: Translating disk, symmetric difference error. Time $t = 100$.

Method	E_{sym}
MOF	0.020
CMOF	0.137
PMOF 0	0.121
PMOF 1	0.030
PMOF 2	0.060
PMOF 4	0.038
PMOF 8	0.050

5.3. Rotating Disk

Table 3: Comparison of the symmetric difference error E_{sym} for the three materials after 5 revolutions ($t = 3140$)

	material 1	material 2	material 3
MOF	2.9	2.7	3.9
CMOF	19.3	14.0	18.9
PMOF	19.5	12.1	17.6

Table 4: Cost comparison for the three materials after 5 revolutions ($t = 3140$)
performance profiling times shown in seconds

MOF	reconstruction:	340
	Level set redistancing (MOF):	351
CMOF	reconstruction:	1837
	Level set redistancing (CMOF):	327
PMOF	PMOF reconstruction:	330
	(intercept + slopes + particle advection procedures)	
	Level set redistancing (PMOF):	329

Table 5: Reconstruction cost (per cell)

three materials disk rotation (Step = 6280, $t = 3140$)

Note: the PMOF reconstruction only involves the intercept calculation.

MOF	iterations to converge:	6.9
	CPU time:	0.018
CMOF	iterations to converge:	13.6
	CPU time:	0.13
PLS-MOF	iterations to converge:	0
	CPU time:	0.009

5.4. Zalesak's Disk

Here we compare the three methods on the 2d rigid body rotation test of 'Zalesak's disk' [26]. The problem domain is defined on $[0, 100] \times [0, 100]$. The initial rigid body is a circular disk is centered at (50,75), with a radius of 15. A slot is cut out from the bottom of the disk with width 5 and height 25. And the prescribed velocity field is given by:

$$\begin{cases} u &= -(\pi/314)(y - 50) \\ v &= (\pi/314)(x - 50) \end{cases}$$

Table 6 shows a comparison of symmetric difference error

$$E_{\text{sym}} = |\Omega^{\text{approx}} \cap \Omega^{\text{exact, complement}}| + |\Omega^{\text{approx, complement}} \cap \Omega^{\text{exact}}|, \quad (55)$$

of the MOF, CMOF, and PLSMOF methods after one full rotation ($t = 628.0$) of the disk.

Table 6: Comparison of symmetric difference error (E_{sym}) at $t = 628$.

'GN' indicates the Gauss-Newton optimization slope reconstruction

'N' indicates the number of subdivisions used in the particle procedure.

Figures 21 and 24 show a comparison between PLSMOF and MOF/CMOF after one full rotation of the disk.

Δx	Δt	MOF GN	CMOF GN	PLSMOF $N = 4$
$\frac{100}{96}$	$\frac{628.0}{1155}$	6.8	19.0	16.8
$\frac{100}{192}$	$\frac{628.0}{2066}$	2.5	7.3	6.48

Table 7: Cost comparison of combined centroid error minimization and intercept calculation

Reconstruction cost: (average number of iterations (GN), reconstruction time).

Note: the PLSMOF reconstruction only involves the intercept calculation.

Δx	Δt	MOF-GN	CMOF-GN	PLSMOF
100/96	628.0/1155	3.6, 0.010	7.3, 0.05	0, 0.009
100/192	628.0/2066	3.7, 0.024	6.7, 0.09	0, 0.019

Table 8: Grid refinement study, PLSMOF, $t = 628$.

‘Coarse’ and ‘fine’ correspond the two grid resolutions used in the previous tables in which the AMR adapts about the interface (interface is fully contained at the appropriate finest level). ‘Curvature’ indicates a curvature-based criterion in which the AMR adapts around regions of high curvature instead. The finest level of the ‘curvature’ case is the same as the ‘fine’ case. Figure ?? shows the mesh adaptation and final interface after one full rotation of the ‘curvature’ case.

refinement:	coarse	fine	curvature
E_{sym}	16.8	6.48	10.34
# particles	5,431	11,295	8,119
# grid cells	3,840	10,240	5,600

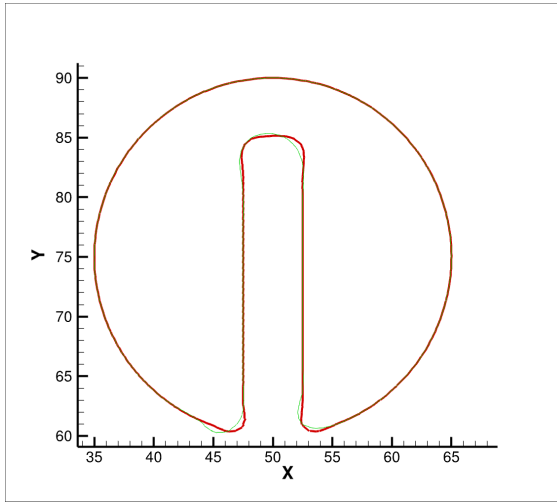


Figure 21: (a)

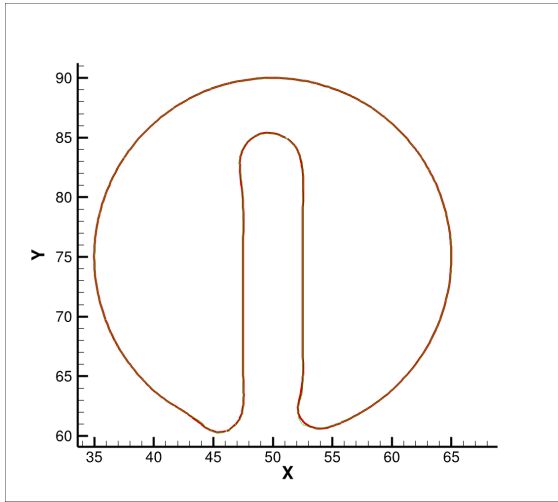


Figure 22: (b)

Figure 23: Zalesak's problem, $t = 628.0$ on a 192^2 grid.

(a) MOF(red) vs. PMOF(green), (b) CMOF(red) vs PMOF(green).

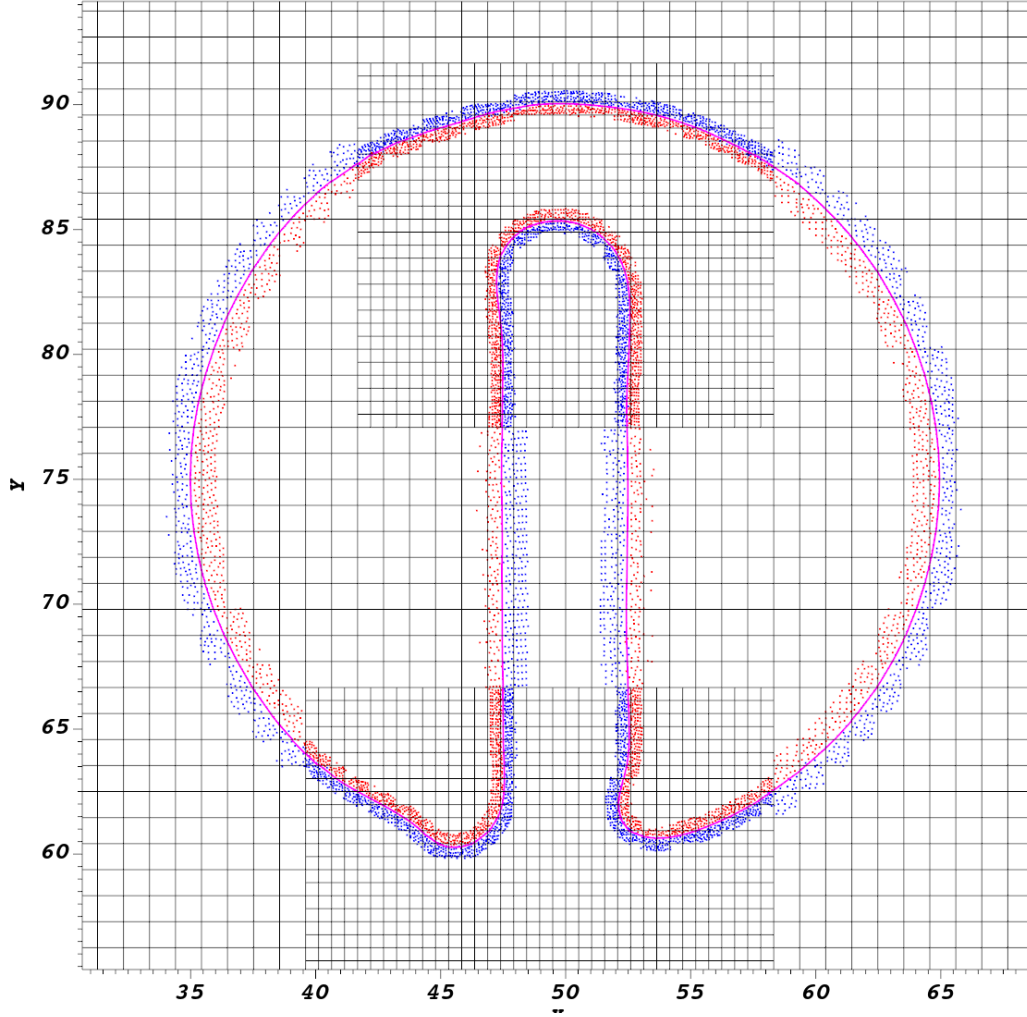


Figure 24: PLSMOF, curvature-based grid refinement, $t = 628.0$, finest grid: 192^2 .
red: interior particles, blue: exterior particles, pink: reconstructed interface
note: particle density is directly tied to the grid resolution.
More figures for this test problem are found in appendix ??.
Remark: particles are contained only on the finest available mesh, in underlying regions and at coarse/fine boundaries, the MOF reconstruction is used instead of the particle-assisted reconstruction.

5.5. Stretching Liquid Lens

Table 9: MOF, CMOF, and PMOF comparison of steady-state major axis length L_0 , measured from the reconstructed interface. L_0^{exact} is the major axis length of the expected steady-state.

Note: This distance is measured as the horizontal distance between the reconstructed triple points of the stretching lens. The numerical solutions may deflect diagonally off-axis and therefore not be a sufficiently representative metric. Figure 29 instead shows the measured perimeter of the lens compared to the analytic solution.

Method	L_0	L_0^{exact}
MOF	0.441	0.460
CMOF	0.468	0.460
PMOF	0.450	0.460

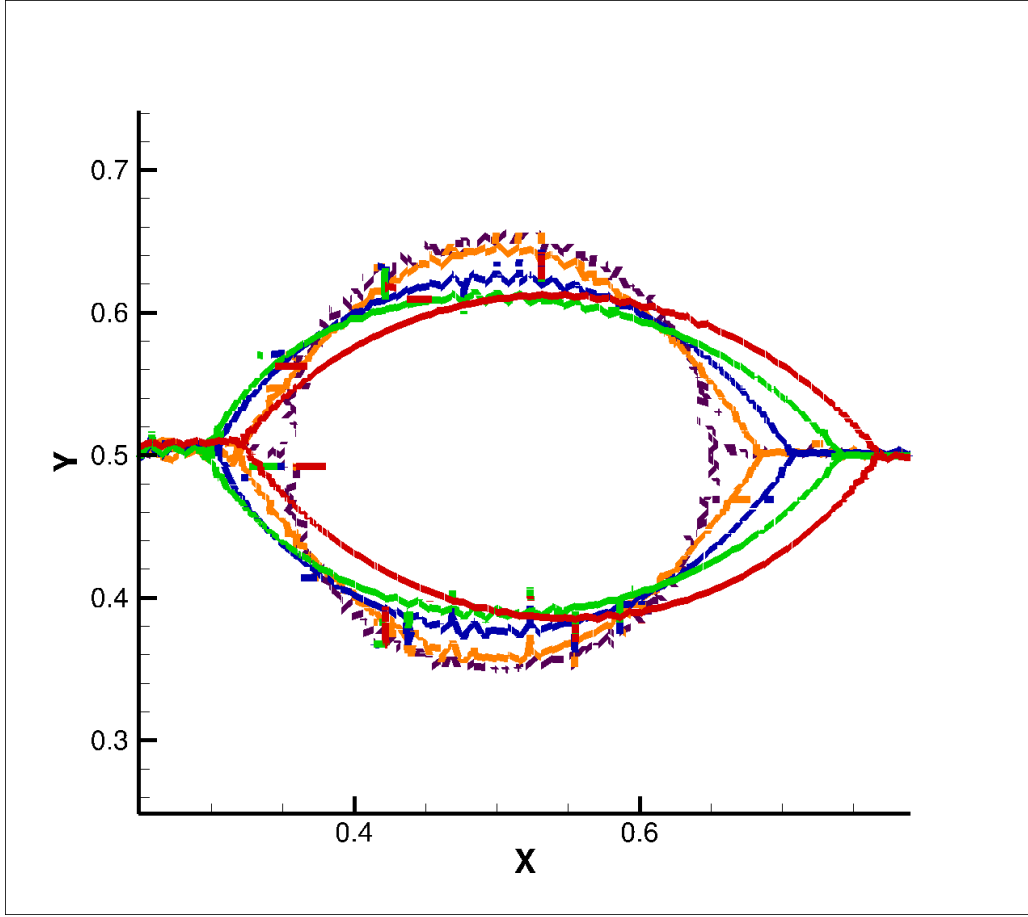


Figure 25: **MOF**, stretching of a liquid lens.

Times shown are:

0.0 (brown), 0.187 (orange), 0.375 (blue), 0.749 (green), and 4.0 (red).

Effective fine grid resolution : $\Delta x_{\text{fine}} = 1/128$.

Initial noise persists.

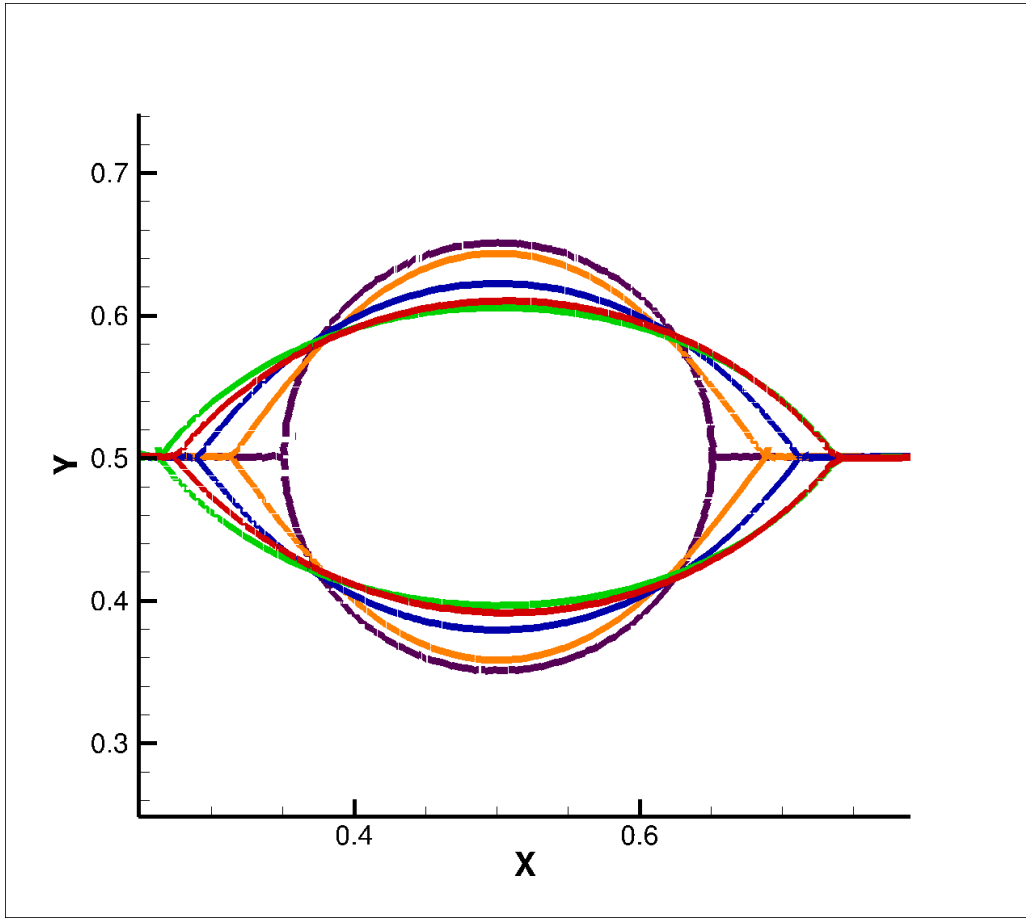


Figure 26: **CMOF**, stretching of a liquid lens.

Times shown are:

0.0 (brown), 0.187 (orange), 0.375 (blue), 0.749 (green), and 4.0 (red).

Effective fine grid resolution : $\Delta x_{\text{fine}} = 1/128$.

Initial noise immediately damped out (c.f. Figure 25).

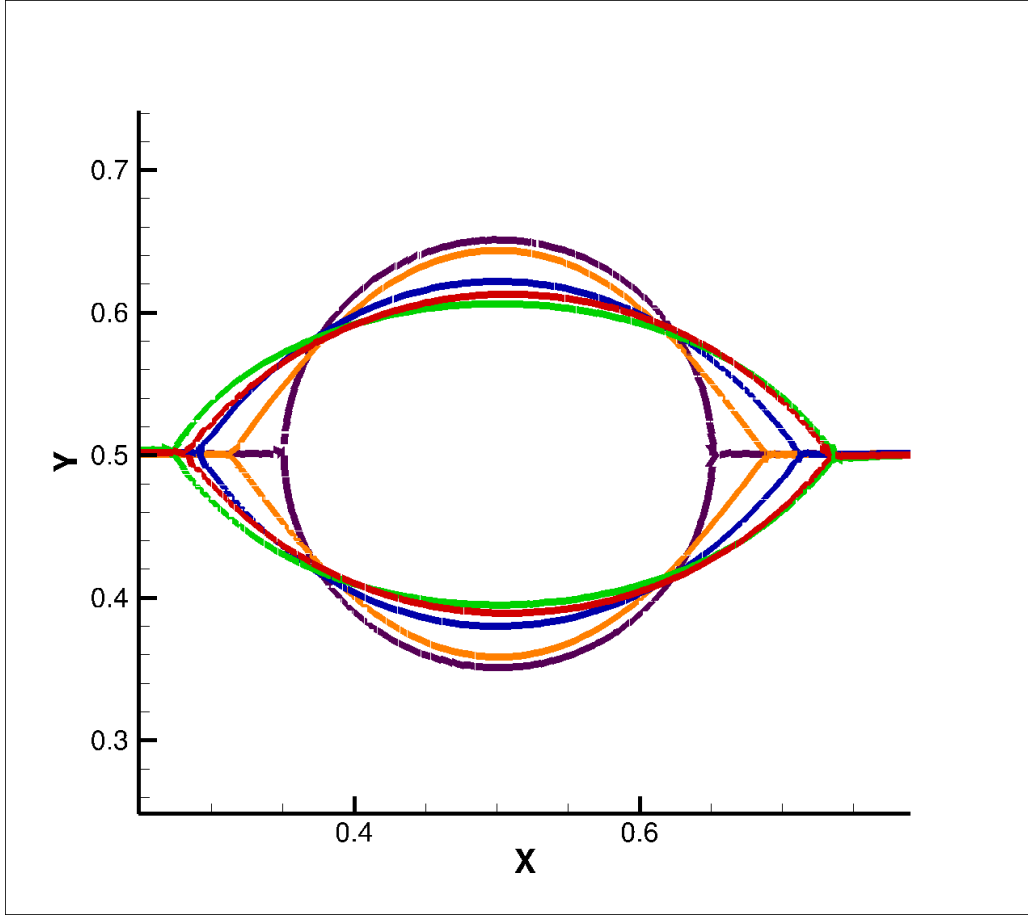


Figure 27: **PMOF** ($N = 4$), stretching of a liquid lens.
 Times $t = 0.0$ (brown), 0.187 (orange), 0.375 (blue), 0.749 (green), and 4.0 (red).
 Effective fine grid resolution : $\Delta x_{\text{fine}} = 1/128$.
 Initial noise immediately damped out (c.f. Figure 25).

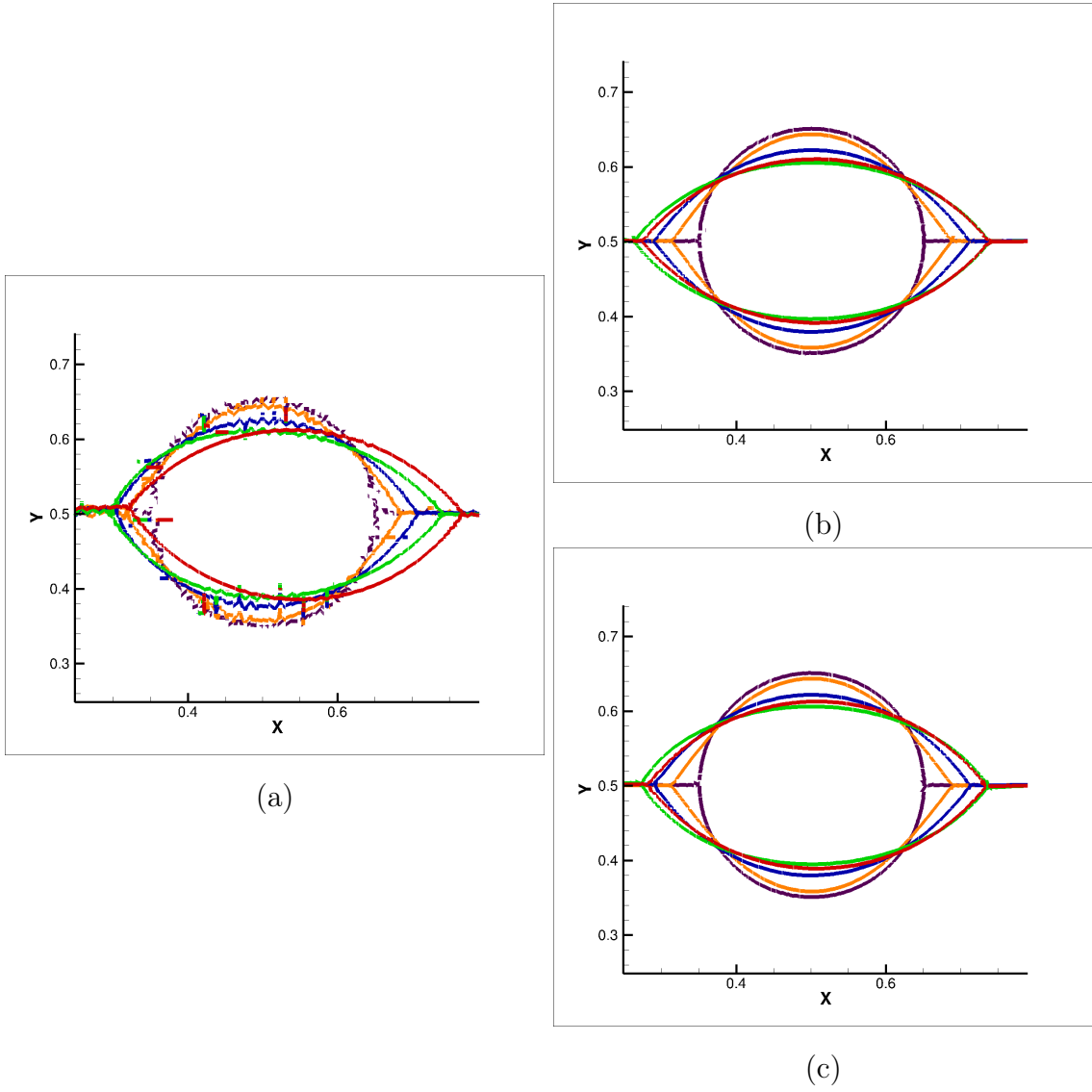


Figure 28: Stretching liquid lense: (a) MOF, (b) CMOF, (c) PMOF ($N = 4$). Times $t = 0.0$ (purple), 0.187 (orange), 0.375 (blue), 0.749 (green), and 4.0 (red). Effective fine grid resolution : $\Delta x_{\text{fine}} = 1/128$.

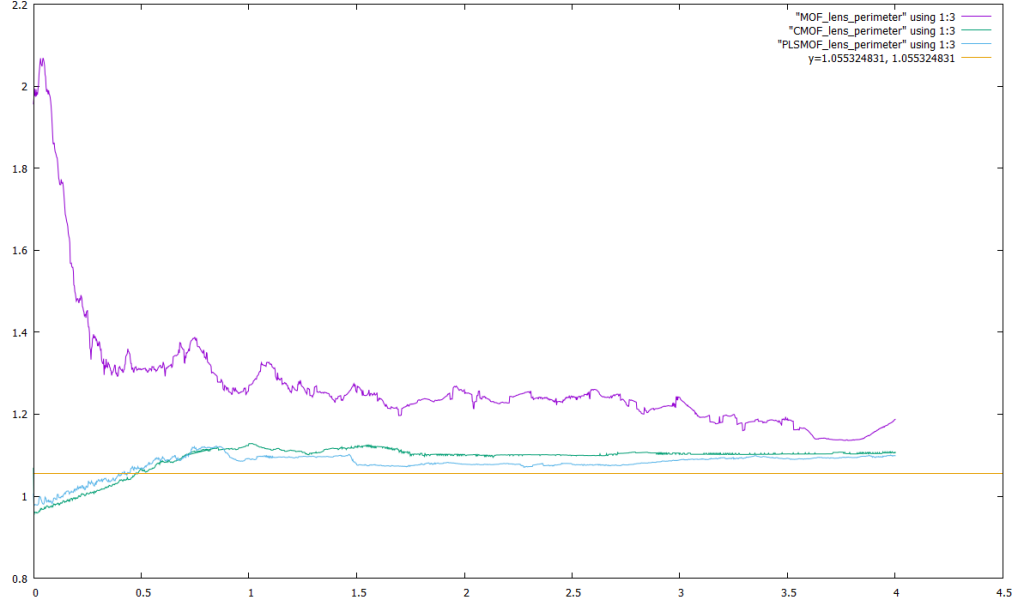


Figure 29: Lens perimeter vs time

purple: MOF, green: CMOF, blue: PMOF, orange: $\mathcal{P}_0^{\text{exact}}$

Note: at the initial time, the perimeter calculation yields a 2% measurement error from top and bottom material initial MOF perimeter measurements, so we expect $\sim 4\%$ error in perimeter measurement.

5.6. Stretching Gas Lens

5.7. Deformation of Spherical Ullage Due to Impinging Jet

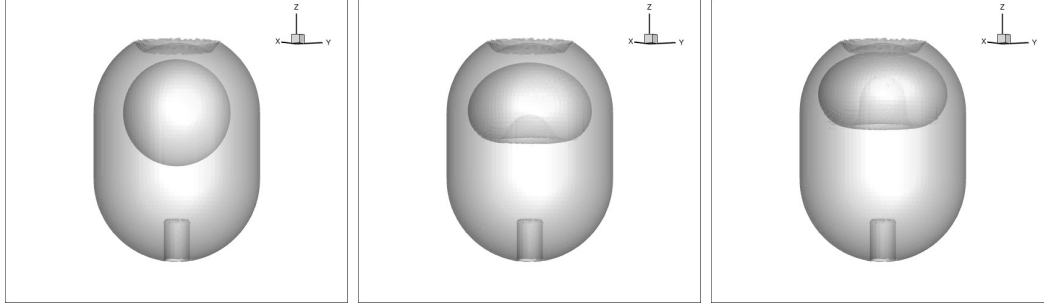


Figure 30: **CMOF**, deformation of a spherical ullage due to a liquid jet, $We_j = 4.875$. Times $t = 0.0, 8.45$, and 15.7 shown. The jet does not penetrate the ullage. Gridsize $64 \times 64 \times 64$. **add above, MOF non-penetrated ullage**

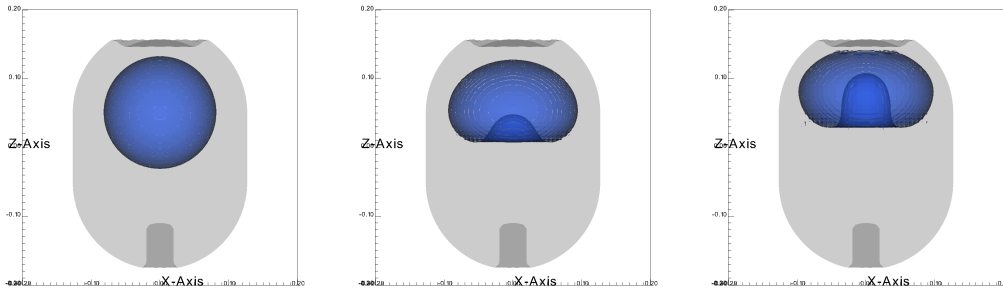
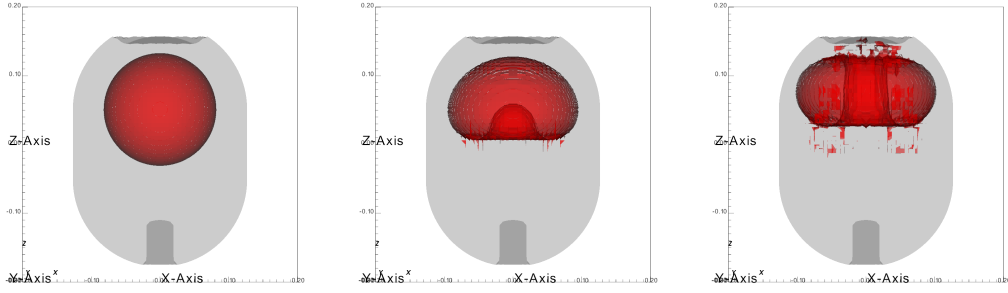
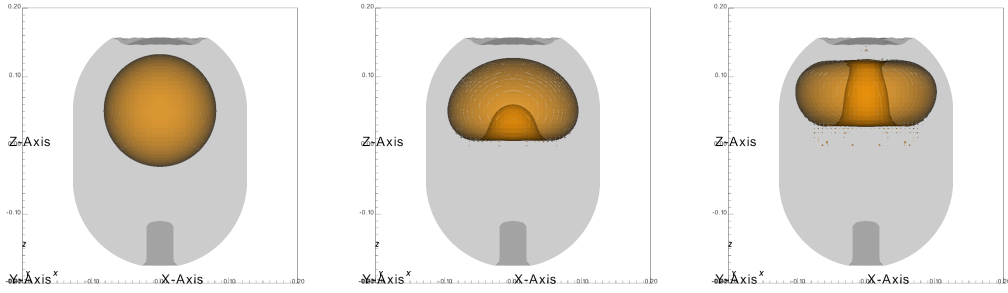


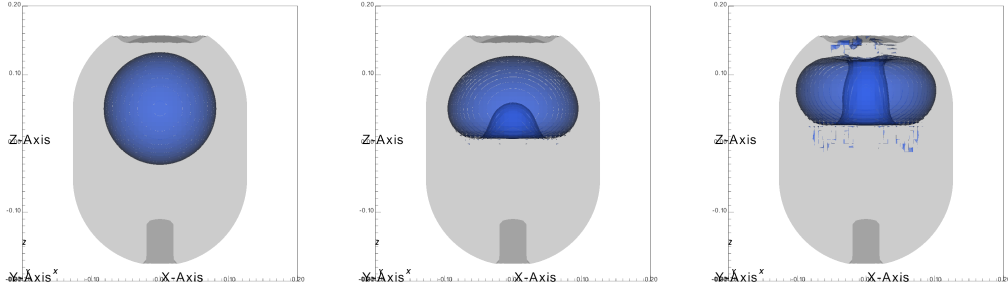
Figure 31: **PMOF**, deformation of a spherical ullage due to a liquid jet, $We_j = 4.875$. Times $t = 0.0, 8.45$, and 15.68 shown. The jet does not penetrate the ullage. Gridsize $64 \times 64 \times 64$.



MOF: Times $t = 0.0, 7.84,$ and $15.51.$



CMOF: Times $t = 0.0, 7.84,$ and $15.83.$



PMOF: Times $t = 0.0, 7.84,$ and $15.60.$

Figure 32: Deformation of a spherical ullage due to a liquid jet, $We_j = 5.25$. Grid size $64 \times 64 \times 64$. Jet penetrates ullage.

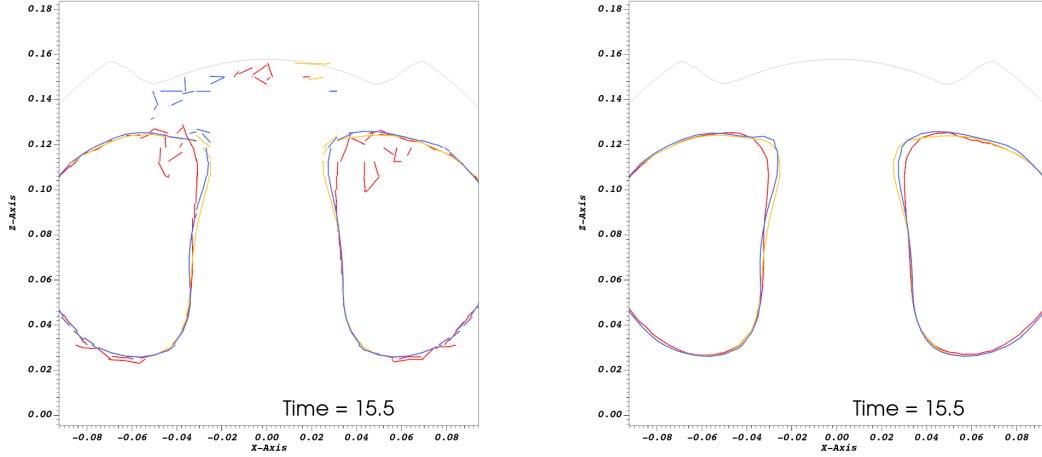


Figure 33: Comparison of vapor/liquid interface. Red: MOF, orange: CMOF, blue: PMOF. **(Left)** Reconstructed interface. **(Right)** Level set.

Appendix A. Example Appendix Section

Appendix text.

References

- [1] ARIENTI, M., AND SUSSMAN, M. An embedded level set method for sharp-interface multiphase simulations of diesel injectors. *International Journal of Multiphase Flow* 59 (2014), 1–14.
- [2] AULISA, E., MANSERVISI, S., SCARDOVELLI, R., AND ZALESKI, S. Interface reconstruction with least-squares fit and split advection in three-dimensional cartesian geometry. *Journal of Computational Physics* 225, 2 (2007), 2301–2319.
- [3] BUKAČ, MARTINA, MUHA, BORIS, AND SALGADO, ABNER J. Analysis of a diffuse interface method for the stokes-darcy coupled problem. *ESAIM: M2AN* 57, 5 (2023), 2623–2658.
- [4] CHORIN, A. J. Numerical solution of the navier-stokes equations. *Mathematics of computation* 22, 104 (1968), 745–762.
- [5] CUMMINS, S. J., FRANCOIS, M. M., AND KOTHE, D. B. Estimating curvature from volume fractions. *Computers & Structures* 83, 6 (2005), 425–434. *Frontier of Multi-Phase Flow Analysis and Fluid-Structure*.

- [6] DE GENNES, P.-G., BROCHARD-WYART, F., AND QUÉRÉ, D. *Capillarity and wetting phenomena: drops, bubbles, pearls, waves*. Springer Science & Business Media, 2013.
- [7] FEDKIW, R. P., ASLAM, T., MERRIMAN, B., AND OSHER, S. A non-oscillatory eulerian approach to interfaces in multimaterial flows (the ghost fluid method). *Journal of computational physics* 152, 2 (1999), 457–492.
- [8] GIBOU, F., FEDKIW, R. P., CHENG, L.-T., AND KANG, M. A second-order-accurate symmetric discretization of the poisson equation on irregular domains. *Journal of Computational Physics* 176, 1 (2002), 205–227.
- [9] KANG, M., FEDKIW, R. P., AND LIU, X.-D. A boundary condition capturing method for multiphase incompressible flow. *Journal of Scientific Computing* 15, 3 (2000), 323–360.
- [10] LI, G., LIAN, Y., GUO, Y., JEMISON, M., SUSSMAN, M., HELMS, T., AND ARIENTI, M. Incompressible multiphase flow and encapsulation simulations using the moment-of-fluid method. *International Journal for Numerical Methods in Fluids* 79, 9 (2015), 456–490.
- [11] LIU, H., KRISHNAN, S., MARELLA, S., AND UDAYKUMAR, H. Sharp interface cartesian grid method ii: A technique for simulating droplet interactions with surfaces of arbitrary shape. *Journal of Computational Physics* 210, 1 (2005), 32–54.
- [12] LIU, Y., SUSSMAN, M., LIAN, Y., HUSSAINI, M. Y., VAHAB, M., AND SHOELE, K. A novel supermesh method for computing solutions to the multi-material stefan problem with complex deforming interfaces and microstructure. *Journal of Scientific Computing* 91, 1 (2022), 1–40.
- [13] LYU, S., WANG, K., ZHANG, Z., PEDRONO, A., SUN, C., AND LEGENDRE, D. A hybrid vof-ibm method for the simulation of freezing liquid films and freezing drops. *Journal of Computational Physics* 432 (2021), 110160.
- [14] MUKUNDAN, A. A., MÉNARD, T., DE MOTTA, J. C. B., AND BERLEMONT, A. A 3d moment of fluid method for simulating complex turbulent multiphase flows. *Computers & Fluids* 198 (2020), 104364.
- [15] PAN, J., LONG, T., CHIRCO, L., SCARDOVELLI, R., POPINET, S., AND ZALESKI, S. An edge-based interface tracking (ebit) method for multiphase-flow

- p>simulation with surface tension.
- Journal of Computational Physics*
- 508 (2024), 113016.
- [16] PEI, C., VAHAB, M., SUSSMAN, M., AND HUSSAINI, M. Y. A hierarchical space-time spectral element and moment-of-fluid method for improved capturing of vortical structures in incompressible multi-phase/multi-material flows. *Journal of Scientific Computing* 81, 3 (2019), 1527–1566.
 - [17] SCARDOVELLI, R., AND ZALESKI, S. Interface reconstruction with least-square fit and split eulerian–lagrangian advection. *International Journal for Numerical Methods in Fluids* 41, 3 (2003), 251–274.
 - [18] STRAIN, J. Semi-lagrangian methods for level set equations. *Journal of Computational Physics* 151, 2 (1999), 498–533.
 - [19] SUSSMAN, M. A second order coupled level set and volume-of-fluid method for computing growth and collapse of vapor bubbles. *Journal of Computational Physics* 187, 1 (2003), 110–136.
 - [20] SUSSMAN, M., SMITH, K. M., HUSSAINI, M. Y., OHTA, M., AND ZHI-WEI, R. A sharp interface method for incompressible two-phase flows. *Journal of computational physics* 221, 2 (2007), 469–505.
 - [21] THAMIL KUMARAN, S., KUMAR, R., AND PREMACHANDRAN, B. A multi-directional advection based moment of fluid method for phase change problems. *Journal of Computational Physics* 508 (2024), 113011.
 - [22] VAHAB, M., SUSSMAN, M., AND SHOELE, K. Fluid-structure interaction of thin flexible bodies in multi-material multi-phase systems. *Journal of Computational Physics* 429 (2021), 110008.
 - [23] WANG, Y., SIMAKHINA, S., AND SUSSMAN, M. A hybrid level set-volume constraint method for incompressible two-phase flow. *Journal of Computational Physics* 231, 19 (2012), 6438–6471.
 - [24] WEYMOUTH, G., AND YUE, D. K.-P. Conservative volume-of-fluid method for free-surface simulations on cartesian-grids. *Journal of Computational Physics* 229, 8 (2010), 2853–2865.
 - [25] YE, Z., ESTEBE, C., LIU, Y., VAHAB, M., HUANG, Z., SUSSMAN, M., MORADIKAZEROUNI, A., SHOELE, K., LIAN, Y., OHTA, M., AND HUSSAINI, M. Y. An Improved Coupled Level Set and Continuous Moment-of-Fluid

Method for Simulating Multiphase Flows with Phase Change. *Communications on Applied Mathematics and Computation* (Aug. 2023).

- [26] ZALESAK, S. T. Fully multidimensional flux-corrected transport algorithms for fluids. *Journal of computational physics* 31, 3 (1979), 335–362.